Tourmaline in a Mesoarchean pelagic hydrothermal system: Implications for the habitat of early life

Tsutomu Ota[a,*], Yuhei Aihara[b], Shoichi Kiyokawa[b], Ryoji Tanaka[a], Eizo Nakamura[a]

[a] *Pheasant Memorial Laboratory for Geochemistry and Cosmochemistry, Institute for Planetary Materials, Okayama University, Misasa, Tottori 682-0193, Japan*
[b] *Department of Earth and Planetary Sciences, Kyushu University, Fukuoka 819-0395, Japan*

Abstract

The RNA world hypothesis requires the synthesis of RNA to allow the emergence of life on Earth. Hydrothermal systems have been proposed as potential candidates for constructing complex biomolecules. However, in order to successfully form RNA, it is necessary to stabilize ribose, a RNA carbohydrate component. Borate has been found to stabilize ribose. Therefore, boron rich hydrothermal systems are important environments concerning the origin of life on Earth.

The 3.2-Ga Dixon Island Formation of the West Pilbara Superterrane, Western Australia, is a volcano-sedimentary sequence. The Formation represents a Mesoarchean pelagic hydrothermal system, which formed adjacent to an immature island arc. Fine-grained tourmaline, in addition to biogenic carbonaceous matter and spherulitic and tubular bacteriomorphs, are found in black chert. A boron-rich environment was responsible for the formation of these deposits. To explore the implications of such a boron enriched environment on microbial activity, modes of occurrence and chemical compositions of the tourmaline were examined.

The tourmaline is schorl or dravite of the alkali tourmaline group and the boron isotope compositions range in δ^{11}B from –7.3 to +2.6‰. The tourmaline occurs in microcrystalline quartz matrix of black chert veins that cross cut a volcanic unit and also in a bedded black chert, which overlays the volcanic unit. The volcanic unit contains highly altered zones with hydrothermal veins. The associated lithologic and stratigraphic features suggest that the black chert veins were the conduits for upward moving hydrothermal fluids, which reached the sea floor. Subsequently, the volcanic unit was covered by organic matter-rich cherty sediments that in part were fed, and/or altered, by the hydrothermal

*Corresponding author at: Pheasant Memorial Laboratory for Geochemistry and Cosmochemistry, Institute for Planetary Materials, Okayama University, Misasa, Tottori 682-0193, Japan.

Email address: tsutom@pheasant.misasa.okayama-u.ac.jp (Tsutomu Ota)

fluids.

These results suggest that the origin of boron enrichment to form Dixon Island tourmaline is not the associated sedimentary mineral assemblage, which includes diagenetic clay, low-grade metamorphic mica, and organic matter. Instead, the tourmaline was directly precipitated from hydrothermal fluid, enriched in boron. Furthermore, the hydrothermal fluids had already concentrated the boron, in the Mesoarchean pelagic system, prior to the apex of organic matter production and microbial activity. Our findings support a hypothesis that the boron-enriched hydrothermal environment aided the survival and evolution of early life.

Keywords: Mesoarchean, hydrothermal system, early life, boron, tourmaline

1. Introduction

A model of microbial evolution, based on the sequence comparison of the ribosomal ribonucleic acid (rRNA) gene (Woese, 1987), implied that the last common ancestor of all animals was hyperthermophile. Consequently, hydrothermal systems, both terrestrial and marine, have been proposed as sites of the first metabolic evolution and thus candidates for the birthplace of life (e.g., Brock, 2001; Prieur et al., 2001). Ancient hydrothermal systems preserved in the Early Archean terranes have been investigated (e.g., Appel et al., 2001; Van Kranendonk, 2006; Hofmann, 2011). Biologic activities in the Early Archean have been inferred mainly from bacterial microfossils, carbon and sulfur isotopes of sedimentary organic matter and pyrite in hydrothermal veins and related deposits (e.g., Schopf, 1993; Rosing, 1999; Westall et al., 2001; Ueno et al., 2001, 2004, 2008; Thomazo et al., 2013; Williford et al., 2016).

Meanwhile, the RNA World (Gilbert, 1986) has been debated as an important phase in the transition from purely prebiotic chemistry towards modern deoxyribonucleic acid (DNA) and protein biochemistry. The RNA world hypothesis requires the abiotic formation of RNA for the emergence of life on Earth (e.g., Orgel, 2004; Cafferty and Hud, 2014). However, ribose, a major carbohydrate component of RNA, is chemically unstable. How the first RNA formed has thus been questioned (Larralde et al., 1995), but experimental studies have confirmed that borate can stabilize ribose (e.g., Ricardo et al., 2004; Kim et al., 2011; Furukawa et al., 2013). The major role of borates in prebiotic processes is further supported by experiments, which demonstrate that borates catalyze the synthesis of nucleic acid bases, amino acids and biogenic carboxylic acids from formamide (Saladino et al., 2011). Accordingly, the essentiality of boron for the appearance of life on Earth has been widely accepted (e.g., Scorei, 2012; Furukawa and Kakegawa, 2017). Furthermore, the recent discovery of boron on Mars has opened up new possibilities that life could have arisen on Mars (Gasda et al., 2017).

A present-day issue is whether or not a boron-rich environment to stabilize ribose was available on the early Earth (e.g., Grew et al., 2011; Furukawa

and Kakegawa, 2017). Indeed, a boron mineral, which belongs to the tourmaline supergroup of borosilicates, has been reported from the Archean terranes (Palmer and Slack, 1989; Swihart and Moore, 1989; Chaussidon and Albarede, 1992). The oldest example is tourmaline in metasediment and tourmalinite of the 3.8-3.7 Ga Isua complex, Greenland (Appel, 1995; Chaussidon and Appel, 1997). Recently, the mineralogy and geochemistry of this mineral were re-investigated (Grew et al., 2015; Mishima et al., 2016). In the 3.5-3.3 Ga Barberton greenstone belt, South Africa, tourmaline was found in stromatolitic sediments (Byerly et al., 1986; Byerly and Palmer, 1991; Farber et al., 2015). Therefore, an environment which favored the formation of tourmaline near the rock-water interface, was also suitable for the development of early-life. Additionally, in the 3.5-3.2 Ga Pilbara terrane, Western Australia, tourmaline has been observed in sedimentary rocks, which are enriched in carbonaceous matter and pyrite. Such enrichments imply the presence of biologic activities in the Early Archean (e.g., Kiyokawa et al., 2006; Van Kranendonk et al., 2008).

The 3.2 Ga Dixon Island Formation of the West Pilbara terrane, which is one of the best examples of a Mesoarchean oceanic stratigraphy, contains possible microbial materials (Kiyokawa et al., 2006; Pinti et al., 2009; Kiyokawa et al., 2012). Fine-grained but abundant tourmalines were found in massive black chert and black chert veins belonging to a volcano-sedimentary sequence. The sequence extends laterally over several kilometers (Kiyokawa et al., 2006; Aihara et al., 2013). Carbonaceous matter, pyrite, and tourmaline in the Dixon Island Formation have well preserved primary textural relationships and chemical features. The preservation suggests the phases were not severely affected by the low-temperature hydrothermal alteration of the Dixon Island Formation. The alteration corresponds to the lowest metamorphic grade of the Cleaverville area, West Pilbara (<250 °C at ∼100 MPa; Ohta et al., 1996; Shibuya et al., 2007).

The tourmaline occurs in the microcrystalline quartz matrix of the black chert. The mineral chemistry more directly reflects the characteristics of hydrothermal fluids than other Archean tourmalines, which occur in metamorphosed sedimentary rocks with the detrital particles of crustal lithology. Nonetheless, characteristics in texture and chemical composition of the Dixon Island tourmaline have not been examined in detail, especially when compared to the other examples from the Eoarchean Isua supracrustal belt and the Paleoarchean Barberton greenstone belt.

As an element, boron is a volatile one, readily transported by aqueous fluids, and has two stable isotopes, ^{10}B and ^{11}B. The isotope ratios in terrestrial materials show a variation of ∼100 ‰ in nature (e.g., Palmer and Swihart, 1996). Such a large isotopic fractionation of boron is very useful to study fluid-mediated processes on the Earth's surface, including geothermal deposits and seafloor hydrothermal systems, and to explore the sources of the fluids (e.g., Spivack and Edmond, 1987; Palmer, 1991; Palmer and Swihart, 1996).

Against such backgrounds, we examined modes of occurrence, major element compositions, and boron isotope compositions of tourmalines in the Dixon Island Formation. In this paper, we discuss the formation process of the tourmaline in

the Mesoarchean hydrothermal system and the implications of the tourmaline for the habitat of the early life.

2. Geological setting

The Dixon Island Formation is a volcano-sedimentary sequence. The formation outcrops along the northern coast of Dixon Island and the northwestern coast of the Cleaverville area, on the northwestern margin of the Archean Pilbara craton, Western Australia (Fig. 1). It consists of a basal Komatiite-Rhyolite Tuff Member, which is conformably overlain by a Black Chert Member and a Varicolored Chert Member. It is also conformably overlain by the Port Robinson Basalt (Fig. 2; Kiyokawa et al., 2014). The basalt has been described as the Dixon Pillow Basalt (e.g., Kiyokawa et al., 2006).

Continuous exposures of the Dixon Island Formation along the northern coast of Dixon Island lie within six geologic blocks (DXA, DXB, DXC, DXD, DXE, and DXF; Figs. 1 and 3) that are bounded by right-lateral strike-slip faults (Kiyokawa et al., 2002). Lithologic and stratigraphic features of each block and lateral variations in the lithology have been described in detail by Kiyokawa et al. (2006, 2012).

The Komatiite-Rhyolite Tuff Member is mainly composed of highly altered komatiite lava. The member also contains pale green, silicified, mafic tuff, well-laminated black chert, and white rhyolite tuff. All components are cut by a set of white and black chert veinlets.

The overlying Black Chert Member is composed of a massive black chert, laminated black chert, dark-greenish siliceous shale and laminated tuffaceous chert. All the above lithologies are composed mainly of microcrystalline quartz. A continuous, stromatolite-like biomat layer is preserved in the laminated black chert bed. The biomat layer is formed of fine-grained iron or iron-coated quartz spherule. The age of the formation, determined by a zircon U-Pb age, is 3195 $\pm$ 15 Ma. The zircon was extracted from a white tuff bed corresponding to the uppermost horizon of the Black Chert Member (Kiyokawa et al., 2002).

The Varicolored Chert Member consists of laminated white, red, and black chert, greenish siliceous shale, and a banded iron formation. All the above lithologies contain no detritus such as lithic fragments and quartzo-feldspathic particles of a continental crust origin. This member is subdivided into a lower, greenish chert submember, and an upper, iron-rich, chert submember. The greenish chert submember consists of greenish bedded siliceous shale, dark greenish shale, and grey siliceous shale. The greenish bedded siliceous shale is massive and consists of micaceous minerals without quartz grains or organic matter. The iron-rich chert submember consists of bedded chert and iron-rich chert beds.

Abundant black chert veins cut across the Komatiite-Rhyolite Tuff Member and terminates at the lowest level of the Varicolored Chert Member. In turn, the chert veins are cut by a number of quartz-veins a few μm to several mm in width. The black chert veins are divided into Type 1 and Type 2 veins (Fig. 2; Kiyokawa

et al., 2006, 2012). Type 1 vein contains abundant carbonaceous peloids in a fine-grained quartz matrix, and terminate at the base of the Black Chert Member. They have been interpreted as the feeder channels for hydrothermal fluids that were expelled onto the sea floor to produce the carbonaceous matter-rich deposits of the Black Chert Member (Kiyokawa et al., 2006). On the other hand, Type 2 veins contain less abundant carbonaceous matter. Instead, they contains brecciated wall rock fragments of black chert and silicified volcanic rocks. Type 2 veins locally penetrate massive black cherts of the Komatiite-Rhyolite Tuff and Black Chert members.

The stratigraphy and lithology of the three members in the six geologic blocks (Fig. 3) suggests that the Dixon Island Formation was a Mesoarchean pelagic hydrothermal environment. Furthermore, it likely occurred on the slope of an immature island arc that was deposited during extension (Kiyokawa and Taira, 1998; Kiyokawa et al., 2002, 2006). Kiyokawa et al. (2012) have reconstructed lateral variations in the sedimentary environment of the Dixon Island Formation. Grabens developed locally and were buried under thick beds of the carbonaceous matter-rich deposits. Meanwhile at the peripheral horsts, such deposits were less dominant. Subsequently, silica-rich hydrothermal activity resulted in the deposition of siliceous sediments on the ocean floor (Fig. 4).

The massive black chert Member has been examined intensively along the northern coast of Dixon Island (e.g., Kiyokawa et al., 2012). Some of the black chert are finely layered (Fig. 5e), and composed of black laminae predominated by sulfide granules (<3 μm). Minor amounts of well-crystallized sulfide ($\sim$200 μm), carbonaceous matter, and white laminae of microcrystalline quartz (Fig. 5f) are also present. Microbial materials have been well preserved in the massive black chert of the lower part of the Black Chert Member. The massive black chert contains carbonaceous peloids, and spiral-, rod-, and dendrite-shaped bacterial materials. Total organic carbon (TOC in wt.%) and the carbon isotope composition (δ^{13}C in ‰) differ between the upper and lower part of the Black Chert Member. The TOC is higher and δ^{13}C slightly lighter in the lower massive black chert (TOC ≤ 0.5; $-43 \leq \delta^{13}\mathrm{C} \leq -23$), than those in the overlying laminated chert of the Black Chert Member and the Varicolored Chert Member, and the black chert veins in the Komatiite-Rhyolite Tuff Member (TOC ≤ 0.2; $-41 \leq \delta^{13}\mathrm{C} \leq -15$) (Kiyokawa et al., 2006; Pinti et al., 2009; Kiyokawa et al., 2012, 2014). The carbon isotope signatures suggest that the carbonaceous matter and the bacteriomorphs, in the lower part of the Black Chert Member, could be of biogenic origin. Furthermore, they could have formed close to a low-temperature hydrothermal vent system.

The tourmaline studied here is from the massive black cherts in the lower parts of the Varicolored Chert Member and the Black Chert Member. Additionally, tourmaline was studied from the black chert veins, which cut the Komatiite-Rhyolite Tuff Member (Fig. 3).

3. Methods

Thin sections of the massive black chert and the black chert vein were made for petrographic observation with optical microscopes. The thin sections were trimmed to be 1-inch in size and circular for further examination, including microscopic observation and chemical analysis. All analyses were conducted at the Pheasant Memorial Laboratory for Geochemistry and Cosmochemistry (PML), Institute for Planetary Materials (IPM), Okayama University, Japan.

The thin sections were carbon-coated for back-scattering electron (BSE) imaging, and major element analysis of tourmaline, using a field-emission-type scanning electron microscope (FE-SEM), JSM-7001F (JEOL, Japan), equipped with an energy dispersive X-ray spectrometer (EDX), AZtec X-Max, X-act (Oxford Instruments, UK). The imaging and quantitative analyses were conducted under conditions of 15 kV acceleration voltage, 3 nA beam current, and 50 s integration times. Calibration for quantitative analysis was conducted using natural silicate minerals, and synthetic oxides and alloys of the JEOL reference materials. Wollastonite ($CaSiO_3$) for Si and Ca, rutile (TiO_2) for Ti, corundum (Al_2O_3) for Al, eskolaite (Cr_2O_3) for Cr, hematite (Fe_2O_3) for Fe, nickel oxide (NiO) for Ni, manganosite (MnO) for Mn, periclase (MgO) for Mg, jadeite ($NaAlSi_2O_6$) for Na, and K-feldspar ($KAlSi_3O_8$) for K. For the Astimex standard mount, MINM25-53+FC (Astimex Standards Ltd., Canada), diopside ($CaMgSi_2O_6$) was used for Ca, pentlandite ($(Fe, Ni)_9S_8$) for Ni, and benitoite ($BaTiSi_3O_9$) for Ba. Analytical uncertainties (RSD) estimated by repeatedly analyzing the reference materials are 3.1 % for Ca, 2.5% for Na and Ni, 1.3–1.1% for Al, K, and Ba, and 1.0–0.8% for the other elements.

After the SEM analysis, the thin sections were polished to remove the carbon coating, washed with deionized water, dried in an electric oven, and then gold-coated for secondary-ion mass-spectrometry (SIMS) analysis.

The boron isotopic compositions of tourmaline and elemental abundance of boron in white mica were determined by using SIMS, a modified Cameca ims-5f ion microprobe (Nakano and Nakamura, 2001; Ota et al., 2008a,b), with an O^- primary beam of 5∼16 nA intensity. Secondary positive ions were collected by ion counting using an energy offset of −45 eV from 4.5 kV acceleration.

For the boron abundance analysis, signal acquisition time was 10 s for $^{11}B^+$ and 5 s for $^{30}Si^+$. A spot analysis comprised of 10 cycles in total. The resultant crater sizes were 5∼10 μm in diameter. The elemental abundances were estimated by [Si] on pre-determined sites, obtained by FE-SEM-EDX in advance, and relative ion yield, Y. The Y was obtained by analyzing in-house reference materials of homogenized natural volcanic glass (gl-tahiti: [B]=$12.4\mu g \cdot g^{-1}$) and synthetic glass (gl-NIST-610: [B]=$356\mu g \cdot g^{-1}$) (Nakamura et al., 2012), and expressed as $Y \equiv \{I(^{11}B^+)/I(^{30}Si^+)\}/([B]/[Si])$. In analytical sessions in this study, the typical analytical error was ∼6%, based on reproducibility of repeated analyses of the reference materials.

For the boron isotope analysis, the signal acquisition time was 5 s for $^{10}B^+$ and 3 s for $^{11}B^+$. A spot analysis comprised of 55 cycles in total. The resultant crater sizes were 10∼15 μm in diameter. The mass resolving power,

(M/ΔM) of ∼1000 is required to separate mass peaks of $^{11}B^+$ and $^{10}BH^+$, but application of energy filtering (−45 eV offset) suppressed $^{10}BH^+$ intensities down to three-orders of magnitude lower than $^{11}B^+$ intensities. This results in insignificant interferences (Nakano and Nakamura, 2001); thus, the lower M/ΔM of ∼500 was applied to acquire higher secondary ion intensities in this study. Measured $^{11}B^+/^{10}B^+$ ratios are expressed as follows; $\delta^{11}B^+ = [(I_{^{11}B^+}/I_{^{10}B^+})/(I_{^{11}B^+}/I_{^{10}B^+})_{ref} - 1] \times 10^3$, where $(I_{^{11}B^+}/I_{^{10}B^+})_{ref}$ means NIST SRM951 value (i.e., 4.0530; Nakano and Nakamura, 2001). The relationship between isotope ratio and ion intensity ratio is described as; $\delta^{11}B = \delta^{11}B^+ + k_{IMF}$, where k_{IMF} means instrumental mass fractionation factor, and was estimated by repeated analysis of a reference tourmaline, TO-1 ($\delta^{11}B$=–13.6, Mg/(Fe+Mg)=0.22, Al/(Al+Fe+Mg)=0.85; Nakano and Nakamura, 2001).

Matrix-induced biases on the instrumental mass fractionation are known to occur for isotope analysis by using SIMS. For analysis of boron isotopes in tourmaline, this matrix effect has been evaluated to be minor but was detected among elbaite (Al), schorl (Fe), and dravite (Mg) end-members (e.g., Chaussidon and Albarede, 1992; Nakano and Nakamura, 2001; Farber et al., 2015). Farber et al. (2015) analyzed boron isotopes for reference tourmalines using SIMS. They suggested matrix-induced biases for the reference tourmalines of schorl and dravite. However, their matrix-induced bias estimates ($\leq$ 1‰) are comparable with or smaller than their typical analytical reproducibility for individual reference tourmalines ($\leq$ 1.2‰ in 2σ). Rather the session-to-session variation in k_{IMF} (∼2‰) is significant more than the matrix-induced biases at individual sessions. This is because the acquired ion intensity ratio is sensitive to the instrumental conditions (e.g., Nakano and Nakamura, 2001).

The boron isotope analyses in this study are composed of 15 analytical sessions, and the k_{IMF} fluctuated from session to session, by up to 10‰. The internal precision of a single analysis of the reference tourmaline was 0.8∼1.4‰ (2σ_{mean}) over all analytical sessions. The reproducibility estimated at individual sessions through repeated analyses of the reference tourmaline was 0.6∼2.0‰ (2σ). The session-to-session variation in k_{IMF} is significantly larger than our analytical reproducibility for the reference tourmaline. The procedure for the boron isotope analyses of this study was essentially the same as that established by Nakano and Nakamura (2001). Therefore, the matrix-induced biases at individual sessions in this study would also be less significant, compared to the session-to-session variation. In this study, we regarded the matrix-induced biases to be negligible. Instead, the k_{IMF} was precisely determined at each session by measuring boron isotope ratios of the reference tourmaline before and after measurements of unknown samples, and the instrumental mass fractionation was corrected accordingly.

4. Results

4.1. Tourmaline and associated mineral occurrences

Tourmalines was found mainly in massive black cherts of the Black Chert Member and in black chert veins in the Komatiite-Rhyolite Tuff Member; how-

ever, some tourmaline was also observed in black and gray chert beds and in the siliceous shale beds of the Varicolored Chert Member (Fig. 3).

Tourmaline occurs together with white mica and sulfides (pyrite, and rarely pentlandite) in the matrix of microcrystalline quartz (<10 μm) and carbonaceous matter, but is absent from quartz veins that cut the black chert. Tourmaline is heterogeneously distributed and randomly oriented in the black chert matrix (Figs. 5b–5d). In the layered black chert, it occurs together with sulfide granules and well-crystallized sulfide crystals (Figs. 6g, 6h). Due to the heterogeneous distribution of tourmaline, local modal abundances can be as high as 20%, within a few-mm thick beds. Nevertheless, modal abundances on petrographic thin sections are generally $\leq$ 0.2% over cm sized areas (2×2 $\sim$ 2×3 cm^2) .

Tourmaline is fine-grained (from 30 to 100 μm in size), acicular in shape, and commonly occurs as aggregates of acicular crystals (Figs. 5b–5d, 6a). Tourmaline grains are composed of two domains: A skeletal domain with abundant micro-inclusions of anhedral quartz (1$\sim$3 μm), and a patchy-zoned, chemically heterogeneous domain with rare micro-inclusions of quartz and iron oxides.

White mica occurs as tiny flakes in microcrystalline quartz matrix of the black chert and the black chert vein (Figs. 6d, 6f). Rarely, coarse-grained mica laths are also observed in the matrix (Fig. 6j). Some of the mica flakes occur along rims of tourmaline grains (Figs. 6k, 6l).

4.2. Major element compositions

This study assumes a tourmaline formula to be $XY_3Z_6(BO_3)_3T_6O_{18}(OH)_4$, where the X site is occupied by Na, Ca, K, and/or vacancies; the Y site by Li, Mg, Fe^{2+}, Mn, Al, Cr, Fe^{3+}, Ti; the Z site typically by Al and appreciable amounts of Mg, Fe^{3+}, and Cr, and the T site by Si with minor Al (Henry and Guidotti, 1985; Henry and Dutrow, 1996; Hawthorne and Henry, 1999; Henry and Dutrow, 2012). Elemental abundances obtained using EDX were recalculated according to this formula on the basis of 29 oxygens, as summarized in Table 1, and Fig. 7.

Tourmaline in the black chert vein and the black chert of the Dixon Island Formation is classified as schorl or dravite of alkali tourmaline group, on the basis of the major element compositions (e.g., Hawthorne and Henry, 1999). Tourmaline compositions range in Na and vacancies in X site from 0.51 to 0.97 and 0.01 to 0.55 apfu (atom per formula unit at 29 oxygens), respectively, and in Mg/(Fe+Mg) from 0.37 to 0.81. Tourmaline exhibits no systematic difference within a specific location, but tourmaline in the layered black chert of the DXE block and black chert vein of the DXF block is rich in [Cr_2O_3] up to 3.5 and 2.7 $cg \cdot g^{-1}$, respectively. Most other Dixon Island Formation tourmaline contain [Cr_2O_3] less than 1 $cg \cdot g^{-1}$(Table 1).

The skeletal and patchy-zoned domains have distinctive chemical compositions within a single tourmaline crystal. The skeletal domains tend to be high in X-site vacancies, and low in Na and Mg, compared to the patchy-zoned domains. Within the patchy-zoned domains, the Al- and Mg-rich patches are surrounded

by the Fe-rich tourmalines (Fig. 7). The skeletal-domain compositions, being high in X-site vacancy and low in Mg, are comparable to those of diagenetic and low-grade metamorphic tourmalines (Henry and Dutrow, 1996).

For the white mica, we assumed a dioctahedral mica with a general formula, $XY_2Z_4O_{10}(OH)_2$, where the X site is occupied by interlayer cations of K, Na, Ca, and Ba; the Y site contains octahedral cations of Al, Mg, Fe^{2+}, Mn, Cr, Fe^{3+}, and Ti, and the Z site is typically occupied by tetrahedral cations of Si and Al (e.g., Bailey, 1984). Elemental abundances obtained were recalculated according to this formula on the basis of 11 oxygens (Table 2).

White mica associated with the tourmaline is muscovite ($KAl_3Si_3O_{10}(OH)_2$) with a small amount of celadonite component ($K[Mg,Fe]AlSi_4O_{10}(OH)_2$). In the black chert vein of the DXF block, mica, similar to tourmaline, is rich in $[Cr_2O_3]$ up to 1.5 $cg \cdot g^{-1}$. Other mica of the Dixon Island Formation contains $[Cr_2O_3]$ less than 0.3 $cg \cdot g^{-1}$(Table 2). The mica is heterogeneous in $[B_2O_3]$, ranging from 0.01 to 0.17 $cg \cdot g^{-1}$(Table 2), even within a single grain (Fig. 6j). Nevertheless, their $[B_2O_3]$ are obviously low, compared with the tourmalines ($[B_2O_3]^{cg \cdot g^{-1}}$=10.3–10.8; Table 1).

4.3. Boron isotope compositions

Boron isotope compositions of the Dixon Island tourmaline are summarized in Table 1, and Figs. 6 and 8. The $\delta^{11}B$ values ($-7.3 \sim +2.6$) of the tourmaline are significantly variable according to the total analytical error of $\leq 2‰$ (2σ). In terms of the mode of occurrence, the $\delta^{11}B$ values are concentrated in narrower ranges for the tourmaline in the black chert vein of the Komatiite-Rhyolite Tuff Member ($-5.0 \leq \delta^{11}B \leq -0.1$) than for those in the black chert of the Black Chert Member ($-7.3 \leq \delta^{11}B \leq +2.6$). Tourmaline in the black chert of the Varicolored Chert Member (–4.2 $\leq \delta^{11}B \leq$ –0.1) is comparable in the boron isotope composition to those in the black chert vein of the Komatiite-Rhyolite Tuff Member. Tourmaline in the pyrite-bearing, layered black chert exhibits lower $\delta^{11}B$ values ($-7.3 \sim -3.7$) compared with those in the massive black chert and the black chert vein. Tourmaline associated with well-crystallized, coarse-grained pyrite yielded the lowest $\delta^{11}B$ value (Fig. 6g).

At a scale of a single tourmaline grain, the skeletal cores tend to yield slightly higher $\delta^{11}B$ values (Fig. 8). As a whole, any systematic core-rim variation in $\delta^{11}B$ was not found, but within individual grains, the $\delta^{11}B$ values become slightly lower from the cores to the rims (Fig. 6a). On a geological map scale, the $\delta^{11}B$ values of tourmaline showed no systematic change. However, the tourmaline in the black chert of DXE and DXF blocks showed relatively lower $\delta^{11}B$ values ($-7.3 \sim -3.0$), compared with those of DXA, DXB, and DXC blocks ($-4.4 \sim +2.6$).

The major and minor element compositions (Figs. 9 and 10) of the tourmalines in the black chert veins are homogeneous in composition, when compared with those in the massive and layered black cherts. In addition, the Cr-rich tourmalines are characterized by the low $\delta^{11}B$ values.

5. Discussion

5.1. Formation of tourmaline in the Dixon Island Formation

The rocks of Dixon Island contain convincing evidence for hydrothermal fluid circulation below the ocean floor (Kiyokawa et al., 2006, 2012). Swarms of quartz veins and black chert veins within the Komatiite-Rhyolite Tuff Member were produced by hydrothermal circulation in a zone up to several meters wide. Thick, highly-altered volcanic zones are interpreted as high-temperature, hydrothermal fluid pathways. Black chert veins (Type 1) would have been conduits for the low-temperature seepage of hydrothermal fluids upon the ocean floor. These seepages and hydrothermal vents were subsequently covered by organic matter-rich cherty sediments in the grabens, which was developed in an extensional stress field during and after sedimentation of the Black Chert Member. Consequently, this sequence of events resulted in a feeder/deposit relationship between the black chert veins in the Komatiite-Rhyolite Tuff Member and the massive and layered black cherts of the Black Chert Member (Fig. 11b). The sedimentary environment would be characterized by very low energy, allowing the organic matter-rich black chert to be deposited on a hydrothermally altered volcanic sequence. Subsequently, silica-rich hydrothermal activity dominated, as exemplified by the Type 2 black chert veins. Siliceous sediments were deposited on the ocean floor, which resulted in the large scale distribution of the finely laminated chert of the Varicolored Chert Member (Fig. 11c).

Tourmaline is found in the black chert vein of the Komatiite-Rhyolite Tuff Member, the massive and layered black cherts of the Black Chert Member, and the massive black cherts and greenish siliceous shales of the Varicolored Chert Member. Acicular tourmaline occurs in the microcrystalline quartz matrix of the black chert veins and the massive and layered black cherts. The skeletal domains of the tourmaline contain many micro-inclusions of anhedral quartz. The tourmaline is often accompanied by white mica and pyrite. These associated minerals occur as discrete grains in the matrix or grow along rims of tourmaline grains (Fig. 6). Such textural characteristics suggest that the tourmaline crystallized earlier than adjacent mica, pyrite, and microcrystalline quartz. The white mica, from this study, contains $[B_2O_3]$ up to 0.1 $cg \cdot g^{-1}$. However, the modal proportion is comparable to or less than that of the tourmaline, which contains $[B_2O_3]$ up to 10.8 $cg \cdot g^{-1}$. Organic matter is also a boron reservoir, and kerogen can contain $[B_2O_3]$ up to 0.08 $cg \cdot g^{-1}$ (Williams et al., 2001b; Williams and Hervig, 2004). However, the amounts of carbonaceous material in the black chert and the black chert veins are up to 0.5% in TOC. Consequently, their contribution to the whole-rock boron abundance is similar to that of the micas. Therefore, most of the $[B_2O_3]$ in the black chert and black chert veins is probably stored in the tourmaline. The boron isotope compositions of the tourmaline would dominate those of the black chert and the black chert veins.

These textural and chemical characteristics suggest that the Dixon Island tourmalines are neither detritus, derived from crustal materials, nor overgrowths from the detritus. Instead, they crystallized directly as a primary minerals from silica- and boron-rich hydrothermal fluids, which had circulated within

the Komatiite-Rhyolite Tuff Member. Komatiite is a type of ultramafic volcanic rock derived from the hot and primitive mantle in the Hadean to the early Archean, and is expected to be enriched in boron being an incompatible element, compared to basaltic oceanic crust derived from the modern mantle (e.g., Herzberg, 1992; Herzberg et al., 2010). Therefore, in addition to differentiated rhyolitic rocks, komatiitic rocks of the Komatiite-Rhyolite Tuff Member would have been important reservoirs for the production of boron-rich hydrothermal fluids.

The temperature conditions of the hydrothermal alteration, within the Dixon Island Formation, have been estimated to be as low as 250 °C (e.g., Shibuya et al., 2007). Similarly, hydrothermal acicular tourmaline with chemical compositions of the schorl-dravite series has been reported from modern vapor-dominated geothermal systems, Indonesia ($200 \leq T \leq 300$ °C; Moore et al., 2004; Etzel et al., 2015). Accordingly, the Dixon Island tourmaline would have crystallized under such conditions of the hydrothermal alteration.

5.2. Chemical compositions of the Dixon Island tourmaline

The Dixon Island tourmaline varies to some extent in major and minor elements and boron isotope compositions, but their δ^{11}B values are clustered within a relatively narrow range ($-7.3 \sim +2.6$), compared to the tourmaline in the Eoarchean Isua supracrustal belt ($-25 \leq \delta^{11}B \leq +6$; Chaussidon and Appel, 1997; Grew et al., 2015) and that in the Paleoarchean Barberton greenstone belt ($-21 \leq \delta^{11}B \leq +10$; Byerly and Palmer, 1991; Farber et al., 2015). This wide spread in δ^{11}B values was probably due to the boron isotope characteristic of the early Archean tourmaline. The tourmaline was likely influenced by chemical variation within the host rocks, which included metamorphosed sedimentary rocks mixed with the detritus of a crustal lithology. In addition, metamorphic tourmaline often has heterogeneous boron isotope compositions, because tourmaline is stable over a wide range of conditions from diagenesis to high-grade metamorphism (e.g., Henry and Dutrow, 1996; Ota et al., 2008a). With increasing metamorphic grade, diagenetic and low-grade metamorphic tourmaline will continue to grow, as long as it coexists with boron-rich low-grade metamorphic minerals such as mica. The tourmaline forms overgrowths by incorporating the boron released from the breakdown of the low-grade metamorphic minerals. In turn, this results in the metamorphic tourmaline containing zoned boron isotope compositions (e.g., Nakano and Nakamura, 2001). Metasedimentary rocks in the Isua supracrustal belt have regionally experienced high-grade metamorphism (440∼590 °C; e.g., Mishima et al., 2016). Consequently, some of the Isua tourmaline have become heterogeneous in both major elements and boron isotope compositions (Grew et al., 2015). The host rocks of the Dixon Island tourmaline are black cherts and siliceous shales, which contain no detritus, such as lithic fragments and quartzo-feldspathic particles of continental crust origin. Additionally, the Dixon Island tourmaline experienced low-temperature hydrothermal alteration (e.g., Shibuya et al., 2007). Therefore, the Dixon Island tourmaline reflects more directly the characteristics of the hydrothermal

fluid, compared with tourmaline from the Isua supracrustal belt and the Barberton greenstone belt. Nonetheless, the chemical variation in the Dixon Island tourmaline is influenced by crustal materials via hydrothermal fluids during diagenesis and low-grade metamorphism.

In the eastern blocks (DXD, DXE, and DXF), the black cherts overlay thick beds of the white tuff, are penetrated by the Type 2 black chert veins and overlain by the greenish siliceous shale. Meanwhile in the western blocks (DXB and DXC), thick beds of the black cherts are intercalated with thin layers of the white tuff and directly overlain by the iron-rich bedded chert. In the westernmost part of the DXA block, thin beds of the black chert with white tuff intercalations are covered by the iron-rich bedded chert (Figs. 3 and 4). The volumetric proportions of volcanic materials to black chert, for the Black Chert Member and the Varicolored Chert Member, are higher in the eastern part of the Dixon island compared to those of the western part. Consequently, the hydrothermal fluids in the eastern part would have been enriched in chemical components derived from the volcanic materials. The resultant silica deposits would have formed during sedimentation of the Black Chert Member and the Varicolored Chert Member (Figs. 11b and 11c). The tourmaline and associated mica from DXE and DXF blocks are rich in [Cr_2O_3], compared with the other tourmaline and mica (Fig. 10 and Table 2). In the Komatiite-Rhyolite Tuff Member, altered komatiite lava and tuff contain Cr-rich spinel (e.g., Kiyokawa et al., 2012); thus, the Cr-rich compositions of tourmaline and mica from the eastern blocks are most likely inherited from the komatiitic rocks containing Cr-rich spinel through interaction with the hydrothermal fluids (Figs. 11b and 11c).

The tourmaline in the black chert veins varies less in δ^{11}B ($-5.0 \sim -0.1$) than that in the black chert ($-7.3 \sim +2.6$). As mentioned earlier, the tectonic setting of the Dixon Island Formation has been reconstructed to be a Mesoarchean pelagic hydrothermal environment adjacent to an immature island arc (e.g., Kiyokawa and Taira, 1998; Kiyokawa et al., 2002). The high-temperature hydrothermal fluids originated from paleo-seawater, which circulated within the Komatiite-Rhyolite Tuff Member. The fluids absorbed chemical components including boron, silica, and chromium, from wall rocks along the fluid pathways.

The δ^{11}B values of the hydrothermal fluids would have decreased, compared to seawater, through interactions between the circulating seawater and the komatiitic and rhyolitic rocks. It is well known that large-scale boron exchange between seawater and the oceanic crust occurs at modern mid-ocean ridges (e.g., Spivack and Edmond, 1987; Palmer, 1991). The exchange gives rise to variations in the boron isotope compositions of hydrothermal vent fluids and the altered oceanic crust. Boron-rich silica deposits precipitate (black chert of the Black Chert Member) from the hydrothermal fluids, which cool when seeping onto the ocean floor. The silica deposits fill up fluid pathways in the komatiitic and rhyolitic crust (black chert vein of the Komatiite-Rhyolite Tuff Member). Subsequently, the tourmaline crystallizes in the silica deposits. The massive and layered black cherts of the Black Chert Member are composed of mate-

rials which were accumulated on the ocean floor by repeated seepages of the hydrothermal fluids circulated in the Komatiite-Rhyolite Tuff Member. Such materials became enriched in extracted crustal chemical components, compared to the black chert veins, which formed in the hydrothermal fluid pathways. In addition, the hydrothermal fluids seeped on the ocean floor would have repeatedly interacted with the seawater. The resultant silica deposits on the ocean floor (massive and layered black cherts) would have become heterogeneous in boron isotope compositions, compared to those filling up the fluid pathways (black chert vein).

Consequently, we considered that the tourmaline from the black chert veins, of the western blocks (DXA, DXB, and DXC) of the Dixon Island, were the most representative for estimating the boron isotope compositions of the Mesoarchean hydrothermal fluid. The boron isotope compositions of the tourmaline ($-4.4 \leq \delta^{11}\mathrm{B} \leq -0.1$) correspond to those of pelagic clays ($-6.6 \leq \delta^{11}\mathrm{B} \leq +2.8$; Spivack et al., 1987; Ishikawa and Nakamura, 1993) and biogenic siliceous oozes ($-3.8 \leq \delta^{11}\mathrm{B} \leq +4.5$; Ishikawa and Nakamura, 1993) from the modern ocean floor (e.g., Marschall, 2018).

The boron isotope fractionation between silicate minerals and fluids depends on temperature, pressure, and pH. However, temperature is the most well constrained parameter for boron isotope fractionation between tourmaline and fluid (Palmer et al., 1987, 1992; Wunder et al., 2005; Meyer et al., 2008). Additionally, the aforementioned studies examined relatively high temperature hydrothermal alteration. Applying the temperature-dependent boron isotope fractionation between tourmaline and fluid (Meyer et al., 2008) to the hydrothermal alteration of the Dixon Island Formation ($200 \leq \mathrm{T} \leq 300$ °C; Shibuya et al., 2007), $\Delta\delta^{11}\mathrm{B}_{\mathrm{tourmaline-fluid}}$ ranges in ‰ from −5.4 to −3.8. Assuming that the Dixon Island tourmalines crystallized directly from the hydrothermal fluids, the boron isotope compositions of the hydrothermal fluids circulated in the Dixon Island Formation are estimated to be $-0.6 \leq \delta^{11}\mathrm{B} \leq +5.3$.

High-temperature (≈ 300 °C) vent fluids from island arc–trench systems and mid-ocean ridges have been examined for their trace element compositions (e.g., Spivack and Edmond, 1987; Palmer, 1991; You et al., 1994; Yamaoka et al., 2015). Accordingly, we can discuss boron isotope systematics in modern seafloor hydrothermal systems at different geological settings. The boron isotope compositions of the mantle, oceanic and continental crusts (e.g., Marschall et al., 2017), and modern seawater (Spivack and Edmond, 1987) have been estimated to be $-10 \leq \delta^{11}\mathrm{B} \leq -7$ and $\delta^{11}\mathrm{B} = +39.5$, respectively. The $\delta^{11}\mathrm{B}$ values of the vent fluids are within the range of these major reservoirs.

Based on a two-component (vent fluid and seawater) mixing model, Yamaoka et al. (2015) have estimated boron isotope compositions of modern-day end-member vent fluids from sediment-starved hydrothermal systems at back-arc and oceanic island arc settings ($+13.5 \leq \delta^{11}\mathrm{B} \leq +36.1$) and at mid-ocean ridges ($+10.1 \leq \delta^{11}\mathrm{B} \leq +32.6$). Their results suggest that interactions with the oceanic crust in the sediment-starved systems at back-arc and oceanic island arc settings have evolved the boron isotope composition of modern seawater and lowered the $\delta^{11}\mathrm{B}$ values by up to 26‰. Then, it is possible to calculate the boron

isotope composition of the Mesoarchean seawater involved in the hydrothermal alteration of the Dixon Island Formation, by assuming that the boron isotope composition of the oceanic crust, and temperature conditions and water/rock ratios for the hydrothermal alteration are insignificantly deviated from those of the modern sediment-starved systems at back-arc and oceanic island arc settings. Our calculated δ^{11}B values (+25 to +31‰) suggest that the Mesoarchean seawater, involved in the hydrothermal alteration, would have been up to 26‰ higher than that of the circulated hydrothermal fluids. The reconstructed Mesoarchean seawater was lower in δ^{11}B ($\approx +28 \pm 3$) than modern seawater. Previous studies have estimated the Eoarchean seawater composition from the tourmaline chemistry of the Isua metasedimentary rocks ($\delta^{11}\mathrm{B} \approx +18 \pm 19$; Chaussidon and Appel, 1997; Grew et al., 2015). Whilst, our reconstructed δ^{11}B values are within error of the estimated Eoarchean seawater composition, this likely reflects the large uncertainties of the Eoarchean values.

Nonetheless, the boron isotope composition of seawater likely changed between the Eoarchean and Mesoarchean eras. Detrital zircon ages of sandstones (Sawada et al., 2018) suggests that the Hadean to the Paleoarchean time is dominated by primitive continental crusts of an oceanic island arc affinity. In contrast, the Mesoarchean to the Paleoproterozoic time is chracterized by the emergence of embryonic continents, and the Mesoproterozoic time by the development of supercontinents. Therefore, the continental crust contribution to the boron isotope composition of seawater would have been insignificant until the Mesoarchean time. The relatively rapid production of continental crust could have facilitated noticeable changes in boron isotope compositions of continents and seawater between the Archean and the Proterozoic time (e.g., Chaussidon and Albarede, 1992).

5.3. Hydrothermal system characterized by boron-rich fluid

The carbon isotope compositions of organic matter from the Dixon Island Formation black chert veins and black chert, which contain the tourmaline studied here, are consistent with a biogenic origin (e.g., Kiyokawa et al., 2012, 2014). This finding indicates that the environment in which tourmaline formed was also suitable for the development of early life. The potential boron-rich tourmaline precursors, including hydrothermal fluids and other solid materials, should have coexisted with the organic matter. If this was the case, the boron-rich precursors would have been closely related to microbial activity. Therefore, the issue is whether or not the emergence and/or the development of microbes was preceded by the boron-bearing environment.

Previous studies proposed that the tourmaline, from Isua metasedimentary rocks, crystallized boron released by the breakdown of diagenetic clay minerals and organic matters in sediments through hydrothermal alteration followed by low-grade metamorphism (e.g., Chaussidon and Appel, 1997; Grew et al., 2015; Mishima et al., 2016). They assumed that the boron-isotope fractionation occurred between seawater and diagenetic clay in pelagic sediments during precipitation and diagenesis of the clay. It was also assumed that subsequent isotope

fractionation occurred between fluid and tourmaline during low-grade metamorphism. The boron-isotope fractionations between pelagic clay and seawater during precipitation (Ishikawa and Nakamura, 1993; Chaussidon and Appel, 1997) and between mica and fluid during diagenesis and low-grade metamorphism (e.g., Williams et al., 2001a; Wunder et al., 2005) are larger than that between tourmaline and fluid. Furthermore, low δ^{11}B values were observed for kerogen ($-33.1 \sim +0.8$; Williams et al., 2001b; Williams and Hervig, 2004) compared with that of ground water ($+1.8 \sim +32.5$; Davidson and Bassett, 1993; Hogan and Blum, 2003). Accordingly, it was suggested that significant isotope fractionation of boron between organic matter (e.g., aromatic C–B–H bond) and fluid occurred during diagenesis (Williams and Hervig, 2004).

Raman spectroscopy revealed that graphite with signatures of aromatic carbon was included in tourmaline from Isua metasedimentary rocks (Mishima et al., 2016). Similarly, in stromatolite from the Barberton greenstone belt, tourmaline with submicron-sized inclusions of carbonaceous matter was reported (Byerly and Palmer, 1991). The δ^{11}B values of the Isua tourmaline from mica-rich metasedimentary rocks ($-29.2 \sim -9.2$) tend to be lower than those from meta-mafic rocks ($-12.8 \sim +5.8$) (Chaussidon and Appel, 1997; Grew et al., 2015). Barberton greenstone belt tourmaline, from mica-bearing stromatolitic cherts, records boron-isotope compositions that vary widely and are dominated by low δ^{11}B values ($-20.7 \sim +1.6$). Conversely, the boron-isotope composition of tourmaline, from altered basaltic and komatiitic rocks, is concentrated within a narrow range with high δ^{11}B values ($-6.6 \sim +2.2$) (Byerly and Palmer, 1991; Farber et al., 2015). Such boron isotope characteristics probably arise due to differences in the boron isotope composition of tourmaline precursors. The Isua metasedimentary rocks and the Barberton stromatolitic cherts likely contained the low-δ^{11}B precursors including diagenetic clay, low-grade metamorphic mica, and organic matter (e.g., Marschall and Jiang, 2011).

However, the Dixon Island tourmalines have relatively high and homogeneous δ^{11}B values ($-4.4 \sim -0.1$). It is unlikely that the source materials, of the Dixon Island Formation black chert veins, contained abundant isotopically-fractionated boron precursors, such as diagenetic clay and organic matter. Mica and carbonaceous matter modal abundances and tourmaline modes of occurrence, from Dixon Island black chert veins, also suggest that the tourmalines did not crystallized from boron stored in precursor phases. Instead, the tourmaline directly precipitated from the boron-rich hydrothermal fluid. Therefore, it is likely that the boron-rich fluid had already circulated in the hydrothermal system before the apex of biogenic carbonaceous matter production and microbial activity (Fig. 11). In fact, the Dixon Island tourmaline occurs not only in the black chert vein but also at the black chert horizons, below the intercalating biomats and fossil-like structures (Fig.s 3 and 4).

Hydrothermal fluids from Lost City hydrothermal field, off the Mid-Atlantic Ridge, were found to be warm, alkaline, and molecular hydrogen-rich (Kelley et al., 2001, 2005). This discovery gave rise to the idea that the ancient ultramafic rock-hosted hydrothermal activities could sustain molecular hydrogen-driven microbial ecosystems. Experimental and theoretical studies, of ultramafic

komatiite-hosted hydrothermal systems, have suggested that alkaline and molecular hydrogen-rich conditions were present, potentially in the early Archean basalt-hosted hydrothermal systems, and more likely in the Hadean and the early Archean komatiite-hosted systems (e.g., Seyfried et al., 2007; Russell et al., 2010; Shibuya et al., 2015).

As mentioned earlier, komatiitic rocks of the Komatiite-Rhyolite Tuff Member, the Mesoarchean Dixon Island Formation, are expected to be enriched in not only boron, but also magnesium. The magnesium enrichment arises due to their ultramafic nature, such rocks being derived from the hot and primitive mantle during the Archean. The hydrothermal alteration of komatiitic rocks could have led to the production of boron- and magnesium-rich hydrothermal fluids. In addition to the catalytic effects of borates on prebiotic synthesis of ribose, magnesium also plays a special role in prebiotic geochemistry (e.g., Holm, 2012). Ribozymes, are catalytic RNA molecules and have been used to support the RNA World hypothesis, due to their ability to perform self-splicing (Gilbert, 1986). However, the catalytic activity of ribozymes depends on the availability of Mg^{2+} (Kruger et al., 1982).

The Dixon Island tourmaline from the Komatiite-Rhyolite Tuff Member suggests that the boron- and magnesium-rich conditions are also an important characteristic of the environments for prebiotic chemical evolution and the emergence of early life.

6. Conclusions

Modes of occurrence, major element compositions, and boron isotope compositions of the tourmalines from the Mesoarchean Dixon Island Formation, Western Australia, indicate that the Dixon Island tourmaline would have not crystallized from isotopically fractionated boron in precursor materials, such as diagenetic clays, low-grade metamorphic micas, and organic matters. Instead, the tourmaline directly precipitated from boron-rich hydrothermal fluids. Furthermore, hydrothermal tourmalines, characterized by isotopically less fractionated boron, suggest that the Mesoarchean seawater had already circulated to concentrate boron in the hydrothermal system, prior to the prime of organic matter production and microbial activity.

The Mesoarchean pelagic hydrothermal system, as exemplified by the Dixon Island Formation, could have concentrated boron enough to form the tourmaline by seawater circulation in oceanic crust. This implies that boron-enriched hydrothermal environments such as geysers and other terrestrial hydrothermal systems, could have also existed on the ocean floor, even in the Hadean and the early Archean times. Such a finding is important, because these periods were characterized by a limited terrestrial land mass. The results of this study support the hypothesis that a boron-enriched hydrothermal environment helps the survival and evolution of early life, through stabilization of ribose and subsequent formation of RNA.

Acknowledgements

We thank Martin J. Van Kranendonk for his constructive comments on an early version of manuscript, and Luke Steller for his fruitful discussion on implications of boron-enriched geyserite and hydrothermal tourmaline on land. We are grateful to Christian Potiszil for his English editing and constructive comments to improve the manuscript. Constructive reviews by anonymous referees, and editorial handlings by Frances Westall helped to improve the manuscript. Tak Kunihiro, Katsura Kobayashi, and other PML members are also thanked for their analytical helps.

This study was supported in part by JSPS Grant-in-Aid for Scientific Research (26257211 to SK), and includes the results performed as a joint research carried out at IPM, Okayama University, supported by Joint Usage/Research Center program by MEXT, Japan.

References

Aihara, Y., Kiyokawa, S., Ito, T., Ikehara, M., Yamaguchi, K. E., Horie, K., Sakamoto, R., Miki, T., 2013. Field occurrence and lithology of Archean hydrothermal systems in the 3.2 Ga Dixon Island Formation, Western Australia. AGU Fall Meeting Abstracts, V43A–2847.

Appel, P. W. U., 1995. Tourmalinites in the 3800 Ma old Isua supracrustal belt, West Greenland. Precambrian Research 72 (3-4), 227–234.

Appel, P. W. U., Rollinson, H. R., Touret, J. L. R., 2001. Remnants of an Early Archaean (>3.75 Ga) sea-floor, hydrothermal system in the Isua Greenstone Belt. Precambrian Research 112 (1-2), 27–49.

Bailey, S. W., 1984. Classification and structures of the micas. In: Bailey, S. W. (Ed.), Micas. Vol. 13. Reviews in Mineralogy, Mineralogical Society of America, pp. 1–12.

Brock, T. D., 2001. The Origins of Research on Thermophiles. In: Reysenbach, A.-L., Voytek, M., Mancinelli, R. (Eds.), Thermophiles: Biodiversity, Ecology, and Evolution. Kluwer Academic-Plenum Publishers, New York, pp. 1–9.

Byerly, G. R., Lower, D. R., Walsh, M. M., 1986. Stromatolites from the 3,300–3,500-Myr Swaziland Supergroup, Barberton Mountain Land, South Africa. Nature 319 (6053), 489–491.

Byerly, G. R., Palmer, M. R., 1991. Tourmaline mineralization in the Barberton greenstone belt, South Africa: early Archean metasomatism by evaporite-derived boron. Contributions to Mineralogy and Petrology 107 (3), 387–402.

Cafferty, B. J., Hud, N. V., 2014. Abiotic synthesis of RNA in water: a common goal of prebiotic chemistry and bottom-up synthetic biology. Current Opinion in Chemical Biology 22, 146–157.

Chaussidon, M., Albarede, F., 1992. Secular boron isotope variations in the continental crust: an ion microprobe study. Earth and Planetary Science Letters 108 (4), 229–241.

Chaussidon, M., Appel, P. W. U., 1997. Boron isotopic composition of tourmalines from the 3.8-Ga-old Isua supracrustals, West Greenland: implications on the δ^{11}B value of early Archean seawater. Chemical Geology 136 (3-4), 171–180.

Davidson, G. R., Bassett, R. L., 1993. Application of boron isotopes for identifying contaminants such as fly ash leachate in groundwater. Environmental Science & Technology 27, 172–176.

Etzel, T. M., Moore, J. N., Bowman, J. R., Jones, C. G., Intani, R. G., Golla, G., Nash, G., 2015. Tourmaline in Geothermal Systems: An Example From Darajat, Indonesia. GRC Transactions 39, 529–536.

Farber, K., Dziggel, A., Trumbull, R. B., Meyer, F. M., Wiedenbeck, M., 2015. Tourmaline B-isotopes as tracers of fluid sources in silicified Palaeoarchaean oceanic crust of the Mendon Formation, Barberton greenstone belt, South Africa. Chemical Geology 417 (C), 134–147.

Furukawa, Y., Horiuchi, M., Kakegawa, T., 2013. Selective Stabilization of Ribose by Borate. Origins of Life and Evolution of Biospheres 43 (4-5), 353–361.

Furukawa, Y., Kakegawa, T., 2017. Borate and the Origin of RNA: A Model for the Precursors to Life. Elements 13, 261–265.

Gasda, P. J., Haldeman, E. B., Wiens, R. C., Rapin, W., Bristow, T. F., Bridges, J. C., Schwenzer, S. P., Clark, B., Herkenhoff, K., Frydenvang, J., Lanza, N. L., Maurice, S., Clegg, S., Delapp, D. M., Sanford, V. L., Bodine, M. R., McInroy, R., 2017. In situ detection of boron by ChemCam on Mars. Geophysical Research Letters 44 (17), 8739–8748.

Gilbert, W., 1986. Origin of life: The RNA world. Nature 319 (6055), 618–618.

Grew, E. S., Bada, J. L., Hazen, R. M., 2011. Borate Minerals and Origin of the RNA World. Origins of Life and Evolution of Biospheres 41 (4), 307–316.

Grew, E. S., Dymek, R. F., De Hoog, J. C. M., Harley, S. L., Boak, J., Hazen, R. M., Yates, M. G., 2015. Boron isotopes in tourmaline from the ca. 3.7-3.8 Ga Isua supracrustal belt, Greenland: Sources for boron in Eoarchean continental crust and seawater. Geochimica et Cosmochimica Acta 163 (C), 156–177.

Hawthorne, F. C., Henry, D. J., 1999. Classification of the minerals of the tourmaline group. European Journal of Mineralogy 11 (2), 201–216.

Henry, D. J., Dutrow, B. L., 1996. Metamorphic tourmaline and its petrologic applications. In: Anovitz, L. M., Grew, E. S. (Eds.), Reviews in Mineralogy. Vol. 33. Mineralogical Society of America, pp. 503–557.

729 Henry, D. J., Dutrow, B. L., 2012. Tourmaline at diagenetic to low-grade meta-
730 morphic conditions: Its petrologic applicability. Lithos 154 (C), 16–32.

731 Henry, D. J., Guidotti, C. V., 1985. Tourmaline as a petrogenetic indicator
732 mineral - an example from the staurolite-grade metapelites of NW Maine.
733 American Mineralogist 70 (1-2), 1–15.

734 Herzberg, C., 1992. Depth and degree of melting of komatiites. Journal of Geo-
735 physical Research: Solid Earth 97 (B4), 4521–4540.

736 Herzberg, C., Condie, K. C., Korenaga, J., 2010. Thermal history of the Earth
737 and its petrological expression. Earth and Planetary Science Letters 292 (1-2),
738 79–88.

739 Hofmann, A., 2011. Archaean hydrothermal systems in the Barberton green-
740 stone belt and their significance as a habitat for early life. In: Golding, S. D.,
741 Glikson, M. (Eds.), Earliest Life on Earth: Habitats, Environments and Meth-
742 ods of Detection. Springer Science & Business Media, Dordrecht, pp. 51–78.

743 Hogan, J. F., Blum, J. D., 2003. Boron and lithium isotopes as groundwater
744 tracers: a study at the Fresh Kills Landfill, Staten Island, New York, USA.
745 Applied geochemistry 18, 615–627.

746 Holm, N. G., 2012. The significance of Mg in prebiotic geochemistry. Geobiology
747 10 (4), 269–279.

748 Ishikawa, T., Nakamura, E., 1993. Boron isotope systematics of marine sedi-
749 ments. Earth and Planetary Science Letters 117 (3-4), 567–580.

750 Kelley, D. S., Karson, J. A., Blackman, D. K., Früh-Green, G. L., Butterfield,
751 D. A., Lilley, M. D., Olson, E. J., Schrenk, M. O., Roe, K. K., Lebon, G. T.,
752 Rivizzigno, P., the AT3-60 Shipboard Party, 2001. An off-axis hydrothermal
753 vent field near the Mid-Atlantic Ridge at 30° N. Nature 412 (6843), 145–149.

754 Kelley, D. S., Karson, J. A., Fruh-Green, G. L., Yoerger, D. R., Shank, T. M.,
755 Butterfield, D. A., Hayes, J. M., Schrenk, M. O., Olson, E. J., Proskurowski,
756 G., Jakuba, M., Bradley, A., Larson, B., Ludwig, K., Glickson, D., Buckman,
757 K., Bradley, A. S., Brazelton, W. J., Roe, K., Elend, M. J., Delacour, A.,
758 Bernasconi, S. M., Lilley, M. D., Baross, J. A., Summons, R. T., Sylva, S. P.,
759 2005. A serpentinite-hosted ecosystem: The Lost City hydrothermal field.
760 Science 307 (5714), 1428–1434.

761 Kim, H.-J., Ricardo, A., Illangkoon, H. I., Kim, M. J., Carrigan, M. A., Frye, F.,
762 Benner, S. A., 2011. Synthesis of carbohydrates in mineral-guided prebiotic
763 cycles. Journal of the American Chemical Society 133 (24), 9457–9468.

764 Kiyokawa, S., Ito, T., Ikehara, M., Kitajima, F., 2006. Middle Archean volcano-
765 hydrothermal sequence: Bacterial microfossil-bearing 3.2 Ga Dixon Island
766 Formation, coastal Pilbara terrane, Australia. Geological Society of America
767 Bulletin 118 (1-2), 3–22.

Kiyokawa, S., Ito, T., Ikehara, M., Yamaguchi, K. E., Koge, S., Sakamoto, R., 2012. Lateral variations in the lithology and organic chemistry of a black shale sequence on the Mesoarchean seafloor affected by hydrothermal processes: The Dixon Island Formation of the coastal Pilbara Terrane, Western Australia. Island Arc 21 (2), 118–147.

Kiyokawa, S., Koge, S., Ito, T., Ikehara, M., 2014. An ocean-floor carbonaceous sedimentary sequence in the 3.2-Ga Dixon Island Formation, coastal Pilbara terrane, Western Australia. Precambrian Research 255, 124–143.

Kiyokawa, S., Taira, A., 1998. The Cleaverville group in the West Pilbara coastal granitoid-greenstone terrain of Western Australia: an example of a Mid-Archaean immature oceanic island-arc succession. Precambrian Research 88 (1-4), 109–142.

Kiyokawa, S., Taira, A., Byrne, T., Bowring, S., Sano, Y., 2002. Structural evolution of the middle Archean coastal Pilbara terrane, Western Australia. Tectonics 21 (5), 1044.

Kruger, K., Grabowski, P. J., Zaug, A. J., Sands, J., Gottschling, D. E., Cech, T. R., 1982. Self-splicing RNA: Autoexcision and autocyclization of the ribosomal RNA intervening sequence of Tetrahymena. Cell 31 (1), 147–157.

Larralde, R., Robertson, M. P., Miller, S. L., 1995. Rates of decomposition of ribose and other sugars: implications for chemical evolution. Proceedings of the National Academy of Sciences 92 (18), 8158–8160.

Marschall, H. R., 2018. Boron isotopes in the ocean floor realm and the mantle. In: Marschall, H. R., Foster, G. L. (Eds.), Boron Isotopes. Springer International Publishing, pp. 189–215.

Marschall, H. R., Jiang, S.-Y., 2011. Tourmaline Isotopes: No Element Left Behind. Elements 7 (5), 313–319.

Marschall, H. R., Wanless, V. D., Shimizu, N., von Strandmann, P. A. E. P., Elliott, T., Monteleone, B. D., 2017. The boron and lithium isotopic composition of mid-ocean ridge basalts and the mantle. Geochimica et Cosmochimica Acta 207, 102–138.

Meyer, C., Wunder, B., Meixner, A., Romer, R. L., Heinrich, W., 2008. Boron-isotope fractionation between tourmaline and fluid: an experimental re-investigation. Contributions to Mineralogy and Petrology 156 (2), 259–267.

Mishima, S., Ohtomo, Y., Kakegawa, T., 2016. Occurrence of tourmaline in metasedimentary rocks of the Isua supracrustal belt, Greenland: Implications for ribose stabilization in Hadean marine sediments. Origins of Life and Evolution of Biospheres 46 (2-3), 247–271.

Moore, J. N., Christenson, B. W., Allis, R. G., Browne, P. R. L., Lutz, S. J., 2004. The mineralogical consequences and behavior of descending acid-sulfate waters: an example from the Karaha–Telaga Bodas geothermal system, Indonesia. The Canadian Mineralogist 42 (5), 1483–1499.

Nakamura, E., Makishima, A., Moriguti, T., Kobayashi, K., Tanaka, R., Kunihiro, T., Tsujimori, T., Sakaguchi, C., Kitagawa, H., Ota, T., Yachi, Y., Yada, T., Abe, M., Fujimura, A., Ueno, M., Mukai, T., Yoshikawa, M., Kawaguchi, J., 2012. Space environment of an asteroid preserved on micrograins returned by the hayabusa spacecraft. Proceedings of the National Academy of Sciences of the United States of America 101, E624–E629.

Nakano, T., Nakamura, E., 2001. Boron isotope geochemistry of metasedimentary rocks and tourmalines in the subduction-zone metamorphism. Physics of Earth Planetary Interiors 127, 233–252.

Ohta, H., Maruyama, S., Takahashi, E., Watanabe, Y., Kato, Y., 1996. Field occurrence, geochemistry and petrogenesis of the Archean Mid-Oceanic Ridge Basalts (AMORBs) of the Cleaverville area, Pilbara Craton, Western Australia. Lithos 37 (2-3), 199–221.

Orgel, L. E., 2004. Prebiotic chemistry and the origin of the RNA world. Critical reviews in biochemistry and molecular biology 39 (2), 99–123.

Ota, T., Kobayashi, K., Katsura, T., Nakamura, E., 2008a. Tourmaline breakdown in a pelitic system: implications for boron cycling through subduction zones. Contributions to Mineralogy and Petrology 155 (1), 19–32.

Ota, T., Kobayashi, K., Kunihiro, T., Nakamura, E., 2008b. Boron cycling by subducted lithosphere; insights from diamondiferous tourmaline from the Kokchetav ultrahigh-pressure metamorphic belt. Geochimica et Cosmochimica Acta 72 (14), 3531–3541.

Palmer, M. R., 1991. Boron isotope systematics of hydrothermal fluids and tourmalines: A synthesis. Chemical Geology 94 (2), 111–121.

Palmer, M. R., London, D., Morgan VI, G. B., Babb, H. A., 1992. Experimental determination of fractionation of $^{11}B/^{10}B$ between tourmaline and aqueous vapor: A temperature- and pressure-dependent isotopic system. Chemical Geology 101 (1-2), 123–129.

Palmer, M. R., Slack, J. F., 1989. Boron isotopic composition of tourmaline from massive sulfide deposits and tourmalinites. Contributions to Mineralogy and Petrology 103 (4), 434–451.

Palmer, M. R., Spivack, A. J., Edmond, J. M., 1987. Temperature and pH controls over isotopic fractionation during adsorption of boron on marine clay. Geochimica et Cosmochimica Acta 51 (9), 2319–2323.

Palmer, M. R., Swihart, G. H., 1996. Boron isotope geochemistry; an overview. In: Anovitz, L. M., Grew, E. S. (Eds.), Reviews in Mineralogy. Vol. 33. Mineralogical Society of America, pp. 709–744.

Pinti, D. L., Hashizume, K., Sugihara, A., Massault, M., Philippot, P., 2009. Isotopic fractionation of nitrogen and carbon in Paleoarchean cherts from Pilbara craton, Western Australia: Origin of ^{15}N-depleted nitrogen. Geochimica et Cosmochimica Acta 73 (13), 3819–3848.

Prieur, D., Voytek, M., Jeanthon, C., Reysenbach, A.-L., 2001. Deep-sea thermophilic prokaryotes. In: Reysenbach, A.-L., Voytek, M., Mancinelli, R. (Eds.), Thermophiles: Biodiversity, Ecology, and Evolution. Kluwer Academic-Plenum Publishers, New York, pp. 11–22.

Ricardo, A., Carrigan, M. A., Olcott, A. N., Benner, S. A., 2004. Borate minerals stabilize ribose. Science 303 (5655), 196.

Rosing, M. T., 1999. ^{13}C-depleted carbon microparticles in >3700-Ma sea-floor sedimentary rocks from West Greenland. Science 283 (5402), 674–676.

Russell, M. J., Hall, A. J., Martin, W., 2010. Serpentinization as a source of energy at the origin of life. Geobiology 8 (5), 355–371.

Saladino, R., Barontini, M., Cossetti, C., Di Mauro, E., Crestini, C., 2011. The Effects of Borate Minerals on the Synthesis of Nucleic Acid Bases, Amino Acids and Biogenic Carboxylic Acids from Formamide. Origins of Life and Evolution of Biospheres 41 (4), 317–330.

Sawada, H., Isozaki, Y., Sakata, S., Hirata, T., Maruyama, S., 2018. Secular change in lifetime of granitic crust and the continental growth: A new view from detrital zircon ages of sandstones. Geoscience Frontiers 9 (4), 1099–1115.

Schopf, J. W., 1993. Microfossils of the Early Archean Apex chert: New evidence of the antiquity of life. Science 260 (5108), 640–646.

Scorei, R., 2012. Is boron a prebiotic element? A mini-review of the essentiality of boron for the appearance of life on Earth. Origins of Life and Evolution of Biospheres 42 (1), 3–17.

Seyfried, W. E. J., Foustoukos, D. I., Fu, Q., 2007. Redox evolution and mass transfer during serpentinization: An experimental and theoretical study at 200 °C, 500 bar with implications for ultramafic-hosted hydrothermal systems at Mid-Ocean Ridges. Geochimica et Cosmochimica Acta 71 (15), 3872–3886.

Shibuya, T., Kitajima, K., Komiya, T., Terabayashi, M., Maruyama, S., 2007. Middle Archean ocean ridge hydrothermal metamorphism and alteration recorded in the Cleaverville area, Pilbara Craton, Western Australia. Journal of Metamorphic Geology 25 (7), 751–767.

Shibuya, T., Yoshizaki, M., Sato, M., Shimizu, K., Nakamura, K., Omori, S., Suzuki, K., Takai, K., Tsunakawa, H., Maruyama, S., 2015. Hydrogen-rich hydrothermal environments in the Hadean ocean inferred from serpentinization of komatiites at 300 °C and 500 bar. Progress in Earth and Planetary Science 2 (1), 46.

Spivack, A. J., Edmond, J. M., 1987. Boron isotope exchange between seawater and the oceanic crust. Geochimica et Cosmochimica Acta 51 (5), 1033–1043.

Spivack, A. J., Palmer, M. R., Edmond, J. M., 1987. The sedimentary cycle of the boron isotopes. Geochimica et Cosmochimica Acta 51 (7), 1939–1949.

Swihart, G. H., Moore, P. B., 1989. A reconnaissance of the boron isotopic composition of tourmaline. Geochimica et Cosmochimica Acta 53 (4), 911–916.

Thomazo, C., Nisbet, E. G., Grassineau, N. V., Peters, M., Strauss, H., 2013. Multiple sulfur and carbon isotope composition of sediments from the Belingwe Greenstone Belt (Zimbabwe): A biogenic methane regulation on mass independent fractionation of sulfur during the Neoarchean? Geochimica et Cosmochimica Acta 121 (C), 120–138.

Ueno, Y., Isozaki, Y., Yurimoto, H., Maruyama, S., 2001. Carbon isotopic signatures of individual Archean microfossils(?) from Western Australia. International Geology Review 43, 196–212.

Ueno, Y., Ono, S., Rumble, D., Maruyama, S., 2008. Quadruple sulfur isotope analysis of ca. 3.5 Ga Dresser Formation: New evidence for microbial sulfate reduction in the early Archean. Geochimica et Cosmochimica Acta 72 (23), 5675–5691.

Ueno, Y., Yoshioka, H., Maruyama, S., Isozaki, Y., 2004. Carbon isotopes and petrography of kerogens in similar to 3.5-Ga hydrothermal silica dikes in the North Pole area, Western Australia. Geochimica et Cosmochimica Acta 68 (3), 573–589.

Van Kranendonk, M. J., 2006. Volcanic degassing, hydrothermal circulation and the flourishing of early life on Earth: A review of the evidence from c. 3490-3240 Ma rocks of the Pilbara Supergroup, Pilbara Craton, Western Australia. Earth Science Reviews 74 (3-4), 197–240.

Van Kranendonk, M. J., Philippot, P., Lepot, K., Bodorkos, S., Pirajno, F., 2008. Geological setting of Earth's oldest fossils in the ca. 3.5Ga Dresser Formation, Pilbara Craton, Western Australia. Precambrian Research 167 (1-2), 93–124.

Westall, F., de Wit, M. J., Dann, J., van der Gaast, S., de Ronde, C. E. J., Gerneke, D., 2001. Early Archean fossil bacteria and biofilms in hydrothermally-influenced sediments from the Barberton greenstone belt, South Africa. Precambrian Research 106 (1), 93–116.

Williams, L. B., Hervig, R. L., 2004. Boron isotope composition of coals: a potential tracer of organic contaminated fluids. Applied geochemistry 19 (10), 1625–1636.

Williams, L. B., Hervig, R. L., Holloway, J. R., Hutcheon, I., 2001a. Boron isotope geochemistry during diagenesis. Part I. Experimental determination of fractionation during illitization of smectite. Geochimica et Cosmochimica Acta 65 (11), 1769–1782.

Williams, L. B., Hervig, R. L., Wieser, M. E., Hutcheon, I., 2001b. The influence of organic matter on the boron isotope geochemistry of the gulf coast sedimentary basin, USA. Chemical Geology 174 (4), 445–461.

Williford, K. H., Ushikubo, T., Lepot, K., Kitajima, K., Hallmann, C., Spicuzza, M. J., Kozdon, R., Eigenbrode, J. L., Summons, R. E., Valley, J. W., 2016. Carbon and sulfur isotopic signatures of ancient life and environment at the microbial scale: Neoarchean shales and carbonates. Geobiology 14 (2), 105–128.

Woese, C. R., 1987. Bacterial evolution. Microbiological Reviews 51 (2), 221–271.

Wunder, B., Meixner, A., Romer, R. L., Wirth, R., Heinrich, W., 2005. The geochemical cycle of boron: constraints from boron isotope partitioning experiments between mica and fluid. Lithos 84 (3), 206–216.

Yamaoka, K., Hong, E., Ishikawa, T., Gamo, T., Kawahata, H., 2015. Boron isotope geochemistry of vent fluids from arc/back-arc seafloor hydrothermal systems in the western Pacific. Chemical Geology 392, 9–18.

You, C. F., Butterfield, D. A., Spivack, A. J., Gieskes, J. M., Gamo, T., Campbell, A. J., 1994. Boron and halide systematics in submarine hydrothermal systems: Effects of phase separation and sedimentary contributions. Earth and Planetary Science Letters 123 (1-3), 227–238.

Table 1: Chemical compositions of tourmaline. Units are in $cg \cdot g^{-1}$. Elemental abundances are normalized to a total of 100 $cg \cdot g^{-1}$. n.d. means *not detected*. † Calculated based on the ideal chemical formula of tourmaline. See also text for details.

Sample No.	Spot No.	Remark	SiO_2	TiO_2	Al_2O_3	Cr_2O_3	FeO	NiO	MnO	MgO	CaO	Na_2O	K_2O	B_2O_3†	H_2O†	$\delta^{11}B$
DXA																
5813-18	T01-1	Skeletal	36.8	0.83	30.6	n.d.	10.3	n.d.	n.d.	4.94	n.d.	2.27	n.d.	10.4	3.61	−2.4
	T01-2	Rim	36.9	1.07	30.8	n.d.	9.17	n.d.	n.d.	5.37	0.15	2.33	n.d.	10.5	3.62	−3.9
	T02-1	Core	36.5	0.12	32.9	0.26	7.19	0.21	n.d.	5.61	n.d.	2.87	n.d.	10.6	3.65	−2.0
	T02-2	Rim	36.0	1.57	30.1	0.10	10.3	0.15	n.d.	5.15	0.18	2.40	n.d.	10.4	3.59	−4.2
	T03-1	Skeletal	36.6	0.27	32.7	0.26	8.34	n.d.	n.d.	5.10	n.d.	2.51	n.d.	10.5	3.64	−1.0
	T04-1	Core	36.6	0.15	32.5	0.32	7.81	n.d.	n.d.	5.62	n.d.	2.84	n.d.	10.6	3.64	−1.7
	T04-2	Rim	36.5	0.94	30.8	0.15	9.81	0.11	n.d.	4.98	n.d.	2.60	n.d.	10.5	3.61	−2.0
	T05-1	Skeletal	36.6	n.d.	32.4	n.d.	9.27	0.29	0.15	4.81	n.d.	2.22	n.d.	10.5	3.62	−2.5
	T10-1	Skeletal	37.3	1.28	29.8	0.16	9.60	0.21	n.d.	5.11	0.15	2.23	n.d.	10.5	3.61	−2.2
	T11-1	Core	36.6	0.26	33.4	0.19	6.26	0.38	n.d.	5.83	n.d.	2.74	n.d.	10.6	3.66	−0.7
	T11-2	Rim	38.5	0.72	29.9	n.d.	9.42	0.13	0.12	4.68	n.d.	2.20	n.d.	10.5	3.63	−3.6
	T11-3	Skeletal	36.9	0.32	31.7	0.15	9.40	0.15	n.d.	4.87	n.d.	2.16	n.d.	10.5	3.62	−0.4
	T11-4	Rim	37.3	0.47	31.2	n.d.	9.58	0.20	n.d.	4.93	n.d.	2.11	n.d.	10.5	3.62	−2.6
	T11-5	Skeletal	37.0	0.84	31.3	0.16	8.77	0.10	n.d.	5.14	n.d.	2.46	n.d.	10.5	3.63	−1.7
	T12-1	Rim	36.7	1.31	30.1	n.d.	10.1	n.d.	n.d.	5.20	0.14	2.34	n.d.	10.4	3.60	−3.2
	T13-1	Rim	36.7	0.19	31.6	0.34	8.79	0.26	n.d.	5.24	n.d.	2.62	n.d.	10.5	3.62	−2.3
	T14-1	Skeletal	36.9	1.55	29.6	n.d.	10.2	n.d.	0.19	4.98	0.14	2.29	n.d.	10.4	3.60	−1.4
	T15-1	Skeletal	36.9	0.48	31.7	0.16	8.59	0.22	0.13	5.24	n.d.	2.38	n.d.	10.5	3.63	−2.5
	T22-1	Skeletal	38.3	0.35	30.8	n.d.	9.32	0.20	n.d.	4.71	n.d.	2.08	n.d.	10.5	3.64	−2.4
	T22-2	Skeletal	37.9	0.43	31.2	n.d.	9.63	n.d.	n.d.	4.53	n.d.	2.04	n.d.	10.5	3.63	−3.2
	T23-1	Skeletal	36.4	0.42	31.8	0.12	9.60	0.38	n.d.	4.79	n.d.	2.18	n.d.	10.5	3.61	−0.1
	T24-1	Rim	39.7	0.70	28.1	0.21	10.3	0.39	n.d.	4.48	n.d.	1.86	n.d.	10.5	3.62	−4.1
DXA vein																
7718-20	T06-1	Rim	36.2	0.86	30.1	0.38	10.3	0.31	n.d.	5.10	0.10	2.49	n.d.	10.4	3.59	−2.2
	T07-1	Skeletal	38.2	0.73	29.7	0.19	9.77	0.15	n.d.	4.86	n.d.	2.17	n.d.	10.5	3.62	−3.3
	T10-1	Skeletal	38.4	0.51	29.3	0.40	10.5	n.d.	n.d.	4.59	n.d.	2.12	n.d.	10.5	3.61	−2.2
	T11-1	Skeletal	39.0	0.21	30.6	0.18	9.36	n.d.	n.d.	4.26	n.d.	1.92	n.d.	10.6	3.65	−4.5
	T13-1	Core	36.3	0.49	30.9	0.79	9.60	n.d.	n.d.	5.06	n.d.	2.77	n.d.	10.4	3.60	−2.7
	T16-1	Skeletal	36.7	0.35	31.5	0.38	9.83	n.d.	n.d.	4.84	n.d.	2.30	n.d.	10.5	3.62	−1.0

Table 1: Continued

Sample No.	Spot No.	Remark	SiO_2	TiO_2	Al_2O_3	Cr_2O_3	FeO	NiO	MnO	MgO	CaO	Na_2O	K_2O	$B_2O_3{}^{\dagger}$	$H_2O^{\dagger}$	$\delta^{11}B$
DXB																
5814-01	T01-1	Core	37.6	0.14	34.1	n.d.	3.33	0.16	n.d.	7.15	n.d.	3.00	n.d.	10.8	3.72	−2.6
	T03-2	Core	37.0	0.13	33.7	0.52	5.45	0.26	n.d.	6.20	n.d.	2.27	n.d.	10.7	3.69	−2.8
	T04-1	Core	37.0	0.10	34.1	0.68	3.70	0.17	n.d.	6.82	n.d.	2.81	n.d.	10.8	3.71	−4.4
	T06-1	Skeletal	37.7	0.24	32.0	0.38	6.18	0.13	0.12	6.30	0.10	2.52	n.d.	10.6	3.67	−2.0
	T07-1	Core	36.9	n.d.	33.7	0.76	6.06	n.d.	n.d.	6.01	n.d.	1.86	n.d.	10.7	3.69	−3.3
	T09-1	Skeletal	37.0	0.16	32.3	n.d.	7.45	0.37	n.d.	6.10	0.13	2.09	n.d.	10.6	3.66	−3.6
	T10-1	Core	37.9	0.14	33.7	0.32	3.91	n.d.	0.10	6.59	n.d.	2.73	n.d.	10.8	3.72	−3.4
	T12-1	Core	37.0	0.23	33.4	0.45	4.68	n.d.	n.d.	6.94	n.d.	2.77	n.d.	10.7	3.70	−3.0
DXB vein																
5814-09	T01-1	Skeletal	37.7	0.51	30.0	n.d.	10.0	0.22	n.d.	4.92	0.11	2.41	n.d.	10.5	3.61	−3.0
	T02-1	Core	36.5	0.12	32.0	0.45	8.26	n.d.	n.d.	5.61	0.11	2.78	n.d.	10.5	3.63	−2.5
	T05-1	Core	36.2	0.28	32.9	0.15	7.43	0.10	0.12	5.67	n.d.	2.70	n.d.	10.6	3.64	−1.7
	T08-1	Skeletal	37.2	0.27	32.0	n.d.	8.26	0.40	n.d.	5.05	0.15	2.45	n.d.	10.5	3.64	−0.9
	T10-1	Core	36.6	0.36	32.6	0.42	7.06	0.16	n.d.	5.52	n.d.	2.90	n.d.	10.6	3.65	−0.7
	T11-1	Skeletal	36.8	0.33	31.9	n.d.	9.28	n.d.	0.11	4.97	n.d.	2.27	n.d.	10.5	3.63	−0.2
	T12-1	Rim	36.1	1.51	29.9	0.12	10.7	0.16	n.d.	4.96	0.17	2.28	n.d.	10.4	3.58	−3.8
DXC																
1009-17	T02-1	Skeletal	38.5	0.36	30.1	0.77	9.27	n.d.	0.18	4.28	n.d.	2.23	n.d.	10.5	3.63	−2.4
	T02-2	Skeletal	36.4	n.d.	32.8	0.18	10.9	n.d.	n.d.	3.73	n.d.	1.69	n.d.	10.5	3.61	−1.7
	T10-1	Skeletal	36.2	0.43	31.5	0.68	10.1	n.d.	n.d.	4.54	n.d.	2.25	0.13	10.4	3.60	+2.6
	T04-1	Skeletal	36.3	0.32	31.4	0.15	9.98	n.d.	0.11	4.94	n.d.	2.69	0.13	10.4	3.60	+0.7
	T07-1	Skeletal	36.4	0.54	30.8	0.14	10.2	0.15	n.d.	4.78	0.10	2.48	0.16	10.4	3.60	−0.5
	T09-1	Skeletal	36.9	0.36	32.4	0.57	7.09	n.d.	n.d.	5.50	n.d.	2.79	n.d.	10.6	3.66	+1.1
	T18-1	Skeletal	37.7	0.53	30.7	n.d.	9.40	n.d.	n.d.	4.68	n.d.	2.87	n.d.	10.5	3.62	−4.2
	T19-1	Skeletal	38.1	n.d.	31.0	n.d.	9.55	n.d.	n.d.	4.54	n.d.	2.64	n.d.	10.5	3.63	−3.8
	T25-2	Skeletal	36.9	0.44	31.5	n.d.	9.53	n.d.	n.d.	4.79	n.d.	2.71	n.d.	10.5	3.62	+0.4
	T25-1	Core	36.7	0.40	31.3	n.d.	9.78	n.d.	n.d.	4.86	n.d.	2.93	n.d.	10.5	3.61	−2.1
	T25-3	Skeletal	37.2	0.60	31.6	n.d.	8.51	n.d.	n.d.	5.32	n.d.	2.63	n.d.	10.5	3.64	+0.5
	T26-1	Rim	37.9	0.34	31.7	n.d.	9.82	n.d.	n.d.	3.96	n.d.	2.07	n.d.	10.5	3.64	−0.7
	T30-1	Rim	36.5	0.67	30.5	0.72	9.61	n.d.	n.d.	4.95	n.d.	2.95	n.d.	10.4	3.60	+0.4
DXC vein																
1007-01	T01-1	Skeletal	36.9	0.26	31.4	n.d.	9.76	0.23	n.d.	4.63	n.d.	2.48	n.d.	10.5	3.61	−2.6

Table 1: Continued

Sample No.	Spot No.	Remark	SiO_2	TiO_2	Al_2O_3	Cr_2O_3	FeO	NiO	MnO	MgO	CaO	Na_2O	K_2O	$B_2O_3{}^{\dagger}$	$H_2O^{\dagger}$	$\delta^{11}B$
	T02-1	Core	36.2	0.40	31.5	n.d.	9.67	0.18	n.d.	5.22	0.11	2.66	n.d.	10.5	3.61	−1.8
	T03-1	Core	36.3	0.41	32.2	0.30	8.00	0.17	0.10	5.21	0.12	2.84	n.d.	10.5	3.63	−0.5
	T04-1	Skeletal	37.2	0.12	31.8	n.d.	10.2	0.30	n.d.	4.10	n.d.	2.04	n.d.	10.5	3.62	−2.5
	T05-1	Core	36.5	0.29	31.3	0.19	9.24	0.15	n.d.	5.18	0.10	2.84	n.d.	10.5	3.61	−0.1
	T05-2	Core	36.6	0.26	33.0	0.26	6.99	0.27	n.d.	5.45	n.d.	2.80	n.d.	10.6	3.65	−2.2
	T05-3	Rim	37.7	1.11	29.3	0.16	10.7	n.d.	n.d.	4.45	0.16	2.29	n.d.	10.4	3.60	−0.3
	T05-4	Skeletal	38.1	0.34	30.0	n.d.	10.2	0.28	n.d.	4.43	n.d.	2.32	n.d.	10.5	3.61	−1.6
	T06-1	Skeletal	37.1	0.94	29.9	n.d.	10.7	n.d.	n.d.	4.57	n.d.	2.45	n.d.	10.4	3.60	−2.6
	T07-1	Core	36.1	0.53	30.7	1.04	9.56	0.23	n.d.	4.95	n.d.	2.79	n.d.	10.4	3.59	−2.6
DXE layered																
3815-21	T04-1	Core	35.9	0.45	28.3	3.54	10.6	0.16	0.13	4.52	n.d.	2.39	n.d.	10.3	3.55	−6.0
	T06-1	Rim	36.0	0.92	28.9	2.73	10.2	0.10	n.d.	4.43	n.d.	2.57	n.d.	10.3	3.57	−6.8
	T07-1	Core	35.6	1.60	27.8	3.21	10.4	n.d.	n.d.	4.70	n.d.	2.83	n.d.	10.3	3.55	−4.7
	T10-1	Core	36.7	n.d.	32.1	1.30	7.31	n.d.	n.d.	5.06	n.d.	3.04	0.10	10.5	3.64	−6.2
	T10-2	Core	37.2	0.27	31.8	1.06	7.31	0.30	n.d.	4.74	n.d.	2.77	0.14	10.6	3.64	−5.4
	T10-3	Core	36.9	0.22	31.8	0.48	10.9	n.d.	0.23	3.64	n.d.	1.67	n.d.	10.5	3.61	−6.2
	T11-1	Rim	37.1	0.74	29.6	0.95	11.0	n.d.	n.d.	4.01	n.d.	2.32	n.d.	10.4	3.59	−6.1
	T13-1	Core	36.6	0.71	31.6	n.d.	11.1	0.36	n.d.	3.93	n.d.	1.58	n.d.	10.4	3.60	−7.3
	T14-1	Skeletal	37.1	0.49	30.5	0.77	11.0	0.26	n.d.	3.73	0.11	1.91	n.d.	10.4	3.59	−5.5
	T16-1	Skeletal	38.0	0.41	29.4	1.73	9.36	n.d.	n.d.	4.38	n.d.	2.46	n.d.	10.5	3.61	−4.3
	T16-2	Core	36.5	0.35	30.9	2.05	7.53	n.d.	0.10	5.37	n.d.	2.87	n.d.	10.5	3.62	−5.7
	T16-3	Skeletal	36.6	0.43	29.4	2.50	9.61	0.18	n.d.	4.48	n.d.	2.42	n.d.	10.4	3.58	−5.2
	T17-1	Core	35.8	0.32	29.8	2.50	9.54	0.57	0.18	4.70	n.d.	2.52	n.d.	10.3	3.57	−3.7
	T18-1	Rim	37.2	0.21	31.2	1.37	7.19	0.27	n.d.	5.16	n.d.	2.92	0.13	10.5	3.63	−6.6
	T20-1	Rim	36.9	0.45	29.6	1.93	9.16	0.21	n.d.	4.69	0.10	2.67	n.d.	10.4	3.60	−4.1
	T29-1	Rim	36.1	0.80	28.2	1.33	11.4	0.19	n.d.	4.80	n.d.	2.84	n.d.	10.3	3.55	−5.9
	T34-1	Rim	36.5	0.78	29.2	3.12	9.07	0.22	n.d.	4.53	n.d.	2.53	n.d.	10.4	3.59	−6.6
DXE vein																
3815-02	T03-1	Core	36.2	0.64	30.2	0.61	10.6	0.32	n.d.	4.60	0.15	2.47	0.18	10.4	3.58	−4.0
	T10-1	Skeletal	36.5	0.10	32.6	n.d.	10.9	n.d.	0.33	3.63	n.d.	1.70	n.d.	10.5	3.61	−4.0
	T12-1	Core	35.9	0.60	30.3	0.41	11.0	0.12	n.d.	4.73	n.d.	2.63	n.d.	10.4	3.57	−3.0
	T23-1	Core	36.6	0.49	31.1	0.47	9.81	0.46	n.d.	4.61	n.d.	2.34	n.d.	10.4	3.60	−5.0
	T25-1	Rim	36.8	n.d.	32.3	n.d.	11.1	n.d.	0.18	3.43	n.d.	1.75	n.d.	10.5	3.61	−3.0

Table 1: Continued

Sample No.	Spot No.	Remark	SiO_2	TiO_2	Al_2O_3	Cr_2O_3	FeO	NiO	MnO	MgO	CaO	Na_2O	K_2O	$B_2O_3{}^{\dagger}$	$H_2O^{\dagger}$	$\delta^{11}B$
	T28-1	Skeletal	37.0	0.37	30.9	n.d.	10.6	0.24	n.d.	4.14	n.d.	2.30	n.d.	10.4	3.60	−5.0
	T28-3	Core	35.9	n.d.	32.9	0.25	11.6	0.12	0.15	3.10	n.d.	1.68	n.d.	10.4	3.59	−2.2
	T29-1	Skeletal	38.0	0.22	31.6	n.d.	10.4	n.d.	0.22	3.56	n.d.	1.70	n.d.	10.5	3.63	−4.4
	T30-1	Core	35.9	0.39	31.6	0.37	11.1	0.15	n.d.	4.04	n.d.	2.14	n.d.	10.4	3.58	−5.0
	T32-1	Rim	36.6	0.46	29.1	1.68	10.2	n.d.	n.d.	4.70	n.d.	2.85	n.d.	10.4	3.57	−5.0
	T39-1	Core	35.9	0.96	30.6	0.65	10.1	n.d.	n.d.	4.68	0.17	2.67	n.d.	10.4	3.59	−4.7
	T40-1	Skeletal	37.1	0.11	31.6	0.35	10.2	n.d.	n.d.	4.11	n.d.	1.91	0.14	10.5	3.61	−3.1
	T41-1	Skeletal	36.6	0.35	31.3	n.d.	10.8	n.d.	n.d.	4.25	n.d.	2.27	n.d.	10.4	3.60	−4.8
	T42-1	Core	36.6	0.35	31.0	0.18	10.9	n.d.	n.d.	4.48	n.d.	2.27	0.12	10.4	3.60	−4.7
	T43-1	Core	37.9	0.17	33.4	0.24	7.23	n.d.	0.11	4.85	n.d.	1.69	n.d.	10.7	3.68	−4.1
	T46-1	Core	37.1	0.72	31.2	0.57	8.54	n.d.	0.10	4.82	n.d.	2.66	n.d.	10.5	3.63	−3.7
DXF																
3818-03	T02-1	Core	36.3	0.13	33.8	0.52	7.10	0.25	n.d.	5.26	n.d.	2.21	n.d.	10.6	3.66	−3.5
	T06-2	Skeletal	37.1	0.17	32.4	0.14	9.65	0.22	n.d.	4.35	n.d.	1.79	n.d.	10.5	3.63	−4.1
	T08-1	Core	37.0	0.15	33.4	0.27	6.97	n.d.	n.d.	5.33	n.d.	2.48	n.d.	10.6	3.67	−3.0
	T13-1	Core	36.2	0.39	31.7	0.34	9.00	0.14	0.10	5.30	n.d.	2.73	n.d.	10.5	3.61	−5.1
	T14-1	Core	37.0	n.d.	34.4	0.19	5.19	0.22	n.d.	5.55	n.d.	2.90	n.d.	10.7	3.69	−4.5
DXF vein																
7716-54	T01-1	Skeletal	36.8	0.15	31.0	1.65	8.72	0.22	n.d.	4.79	n.d.	2.44	n.d.	10.5	3.62	−2.6
	T02-1	Skeletal	38.4	0.40	30.2	0.28	9.90	n.d.	n.d.	4.54	n.d.	2.07	n.d.	10.5	3.63	−3.6
	T03-1	Skeletal	37.5	0.43	30.4	1.18	9.44	n.d.	n.d.	4.57	n.d.	2.29	n.d.	10.5	3.62	−1.8
	T04-1	Core	35.8	0.22	31.0	1.69	9.34	0.19	0.20	4.93	n.d.	2.52	n.d.	10.4	3.59	−3.6
	T05-1	Core	36.3	0.23	30.7	2.18	8.62	0.28	0.15	4.89	n.d.	2.65	n.d.	10.4	3.60	−4.2
	T06-1	Core	35.9	0.12	31.2	2.71	8.35	0.29	n.d.	4.93	n.d.	2.43	n.d.	10.4	3.60	−4.6
	T09-2	Skeletal	37.2	0.32	31.2	0.95	9.91	0.28	n.d.	4.13	n.d.	1.88	n.d.	10.5	3.62	−2.8

Table 2: Chemical compositions of mica. Units are in $cg \cdot g^{-1}$, except for B_2O_3, which is in $\mu g \cdot g^{-1}$. With the exception of boron, abundances of elements are normalized to a total of 100 $cg \cdot g^{-1}$. n.d. means *not detected*. n.a. means *not analyzed*. † Calculated based on the ideal chemical formula of mica.

Sample No.	Spot No.	Remark	SiO_2	TiO_2	Al_2O_3	Cr_2O_3	FeO	NiO	MnO	MgO	CaO	Na_2O	K_2O	BaO	$H_2O^\dagger$	B_2O_3
DXA vein																
7718-20	M01-02	Core	47.1	0.42	32.1	n.d.	3.59	n.d.	n.d.	1.05	n.d.	0.38	9.95	0.93	4.45	1304
	M01-89	Rim	44.8	n.d.	36.1	0.19	0.23	n.d.	n.d.	0.21	n.d.	0.67	9.11	4.09	4.43	n.a.
	M05-05	Core	48.0	n.d.	34.5	n.d.	1.81	n.d.	n.d.	0.86	n.d.	0.60	9.67	n.d.	4.54	1185
	M05-06	Core	46.9	n.d.	36.7	n.d.	n.d.	n.d.	n.d.	0.27	n.d.	1.05	7.39	3.17	4.53	1623
	M08-09	Core	46.9	0.65	33.4	n.d.	1.94	n.d.	n.d.	1.12	n.d.	0.39	11.1	n.d.	4.49	1536
	M08-107	Rim	44.2	n.d.	37.0	n.d.	0.12	n.d.	n.d.	0.18	n.d.	0.68	8.97	4.22	4.43	n.a.
	M09-12	Core	51.2	n.d.	30.3	n.d.	2.00	n.d.	n.d.	1.40	n.d.	0.23	10.3	n.d.	4.54	840
	M09-109	Rim	45.8	0.12	35.2	0.12	0.26	n.d.	n.d.	0.22	n.d.	0.69	8.81	4.20	4.44	n.a.
	M10-14	Core	49.6	n.d.	31.6	n.d.	2.24	n.d.	n.d.	1.27	n.d.	0.32	9.28	1.13	4.51	934
	M10-118	Rim	45.8	n.d.	35.2	0.19	0.51	n.d.	n.d.	0.54	n.d.	0.63	8.76	3.92	4.44	n.a.
	M11-124	Core	47.2	0.10	34.4	0.10	0.17	n.d.	n.d.	0.20	n.d.	0.58	8.20	4.48	4.46	n.a.
	M14-18	Core	45.4	n.d.	37.5	n.d.	n.d.	n.d.	n.d.	n.d.	n.d.	0.55	8.09	4.01	4.48	1594
	M14-134	Rim	44.5	n.d.	36.2	0.13	0.13	n.d.	n.d.	0.13	0.10	0.71	8.70	4.90	4.41	n.a.
	M16-139	Core	49.6	n.d.	32.8	0.27	0.11	n.d.	n.d.	0.29	n.d.	0.65	8.30	3.38	4.51	n.a.
DXB vein																
5814-09	MM1-20	Core	48.5	n.d.	31.8	n.d.	3.11	n.d.	n.d.	1.80	n.d.	n.d.	10.3	n.d.	4.50	198
	MM2-23	Core	54.4	n.d.	28.1	n.d.	1.79	n.d.	n.d.	0.59	n.d.	0.32	7.77	2.50	4.55	396
	MM3-27	Core	48.6	n.d.	29.5	n.d.	4.11	n.d.	n.d.	2.45	n.d.	0.25	10.0	0.60	4.45	199
	M03-68	Core	50.1	0.18	31.5	n.d.	0.39	n.d.	n.d.	0.37	n.d.	0.47	7.87	4.43	4.48	n.a.
	MM4-28	Core	46.5	n.d.	35.9	n.d.	1.97	n.d.	n.d.	0.44	n.d.	0.84	9.89	n.d.	4.52	769
	MM5-30	Core	47.2	0.46	33.0	n.d.	3.14	n.d.	n.d.	0.89	n.d.	0.22	10.7	n.d.	4.48	1712
	MM6-31	Core	49.3	n.d.	32.8	n.d.	2.14	n.d.	n.d.	1.72	n.d.	0.22	9.31	n.d.	4.55	1503
	MM7-33	Core	45.8	n.d.	34.4	n.d.	2.64	n.d.	n.d.	0.80	n.d.	0.24	11.7	n.d.	4.46	353
	MM8-36	Core	46.9	n.d.	33.1	n.d.	3.27	n.d.	n.d.	1.16	n.d.	0.30	10.9	n.d.	4.47	458
DXC vein																
1007-01	M03-154	At tour rim	49.5	0.16	31.9	0.24	1.04	n.d.	n.d.	0.80	n.d.	0.24	11.0	0.55	4.51	n.a.
	M03-156	At tour rim	50.3	0.52	29.6	0.13	4.48	n.d.	n.d.	2.16	0.15	0.94	7.06	n.d.	4.54	n.a.
	M04-167	At tour rim	47.7	0.53	32.5	n.d.	2.90	n.d.	n.d.	1.70	0.14	0.53	9.45	n.d.	4.51	n.a.
	M04-168	At tour rim	48.7	0.35	31.7	n.d.	1.90	0.12	n.d.	1.40	n.d.	0.33	10.9	n.d.	4.50	n.a.

Table 2: Continued

Sample No.	Spot No.	Remark	SiO_2	TiO_2	Al_2O_3	Cr_2O_3	FeO	NiO	MnO	MgO	CaO	Na_2O	K_2O	BaO	$H_2O^{\dagger}$	B_2O_3
	M06-187	At tour rim	48.7	0.36	32.3	n.d.	1.04	n.d.	n.d.	1.05	0.10	0.31	11.5	n.d.	4.51	n.a.
	M06-188	At tour rim	49.9	0.12	31.5	n.d.	1.48	n.d.	n.d.	0.81	n.d.	0.33	11.2	n.d.	4.52	n.a.
DXE vein																
3815-02	M01-01	Rim	46.5	n.d.	32.6	0.13	1.44	n.d.	n.d.	1.71	n.d.	0.23	12.4	0.51	4.44	626
	M05-01	Core	46.9	0.28	30.0	n.d.	3.95	n.d.	n.d.	1.60	0.18	0.20	12.2	0.21	4.40	302
	M19-01	Core	46.9	0.16	29.4	n.d.	4.27	n.d.	n.d.	1.93	n.d.	0.17	12.0	0.85	4.38	540
	M35-01	Core	43.3	1.34	31.1	n.d.	3.62	0.36	n.d.	1.26	0.16	0.50	11.0	2.99	4.30	103
	M35-02	Rim	46.1	n.d.	35.2	n.d.	0.91	n.d.	n.d.	0.22	n.d.	0.25	12.5	0.14	4.47	657
	M36-01	Core	48.4	n.d.	30.4	n.d.	2.69	n.d.	n.d.	1.39	0.16	0.11	12.1	n.d.	4.45	1016
DXF																
3818-03	M02-12	At tour rim	50.7	0.44	30.9	0.54	3.83	n.d.	0.11	2.26	n.d.	0.93	5.54	n.d.	4.60	n.a.
	M06-03	At tour rim	47.4	0.18	33.6	0.25	1.82	0.16	n.d.	1.26	n.d.	0.70	9.29	0.80	4.50	n.a.
	M06-04	At tour rim	50.2	0.34	30.8	0.17	1.92	0.20	n.d.	1.25	0.11	0.64	9.32	0.56	4.53	n.a.
	M08-28	At tour rim	49.6	0.57	31.7	0.28	2.43	n.d.	n.d.	1.39	0.14	0.59	8.70	n.d.	4.55	n.a.
	M08-29	At tour rim	51.5	0.20	31.4	n.d.	1.21	0.10	0.10	0.89	n.d.	0.63	8.61	0.66	4.57	n.a.
	M14-21	At tour rim	52.4	0.49	29.8	0.41	2.42	n.d.	n.d.	1.18	n.d.	0.63	8.03	n.d.	4.59	n.a.
DXF vein																
7716-54	M01-12	Core	53.1	n.d.	29.7	0.77	0.47	n.d.	0.16	0.47	n.d.	0.68	9.64	0.42	4.57	n.a.
	M01-39	Core	52.9	n.d.	31.2	0.57	0.52	n.d.	n.d.	0.47	n.d.	0.41	8.64	0.75	4.60	634
	M02-23	At tour rim	47.9	0.11	33.1	0.81	0.85	n.d.	0.10	0.49	0.10	0.38	11.1	0.62	4.49	n.a.
	M03-34	At tour rim	47.5	n.d.	33.6	0.81	0.89	n.d.	0.10	0.68	n.d.	0.41	10.9	0.48	4.50	n.a.
	M04-45	At tour rim	50.0	0.19	31.6	0.91	0.80	n.d.	0.14	0.78	n.d.	0.37	10.6	n.d.	4.54	n.a.
	M05-57	At tour rim	46.2	0.33	35.1	0.52	0.86	n.d.	n.d.	0.59	n.d.	0.41	11.5	n.d.	4.49	n.a.
	M06-41	Core	46.6	n.d.	35.1	1.16	0.61	n.d.	n.d.	0.49	n.d.	0.45	10.4	0.62	4.51	779
	M06-65	At tour rim	47.0	0.14	34.2	0.83	0.66	0.12	0.11	0.61	n.d.	0.56	10.7	0.45	4.50	n.a.
	M07-74	At tour rim	46.6	0.15	33.6	1.36	1.60	n.d.	n.d.	1.21	n.d.	0.66	9.83	0.41	4.49	n.a.
	M09-44	Core	48.5	n.d.	34.3	1.02	0.52	n.d.	n.d.	0.43	n.d.	0.53	9.32	0.78	4.55	515
	M09-83	At tour rim	49.6	0.45	30.6	0.76	1.39	n.d.	n.d.	0.92	n.d.	0.32	11.2	n.d.	4.50	n.a.
	MM1-46	Core	46.4	n.d.	36.1	1.20	n.d.	n.d.	n.d.	0.42	n.d.	0.45	9.65	1.17	4.52	927
	MM2-50	Core	47.5	n.d.	35.5	0.76	0.50	n.d.	n.d.	0.48	n.d.	0.36	10.3	n.d.	4.55	618
	MM3-52	Core	46.2	n.d.	35.0	1.10	2.22	n.d.	n.d.	0.53	n.d.	0.36	9.07	1.11	4.49	1472
	MM4-55	Core	47.2	n.d.	36.5	1.53	n.d.	n.d.	n.d.	0.41	n.d.	0.41	8.21	1.16	4.56	1378

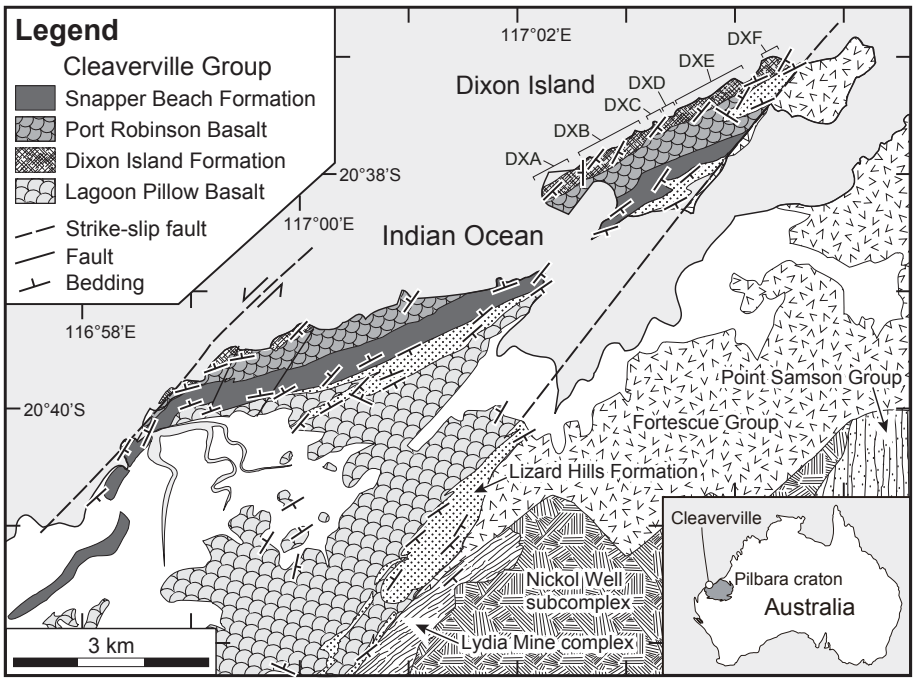

Figure 1: Geological map of the Cleaverville area, which is situated on the northwestern margin of the Pilbara craton, Western Australia, simplified after Kiyokawa et al. (2006, 2014). Localities of structural blocks of DXA, DXB, DXC, DXD, DXE, and DXF along the Dixon Island coast are also shown.

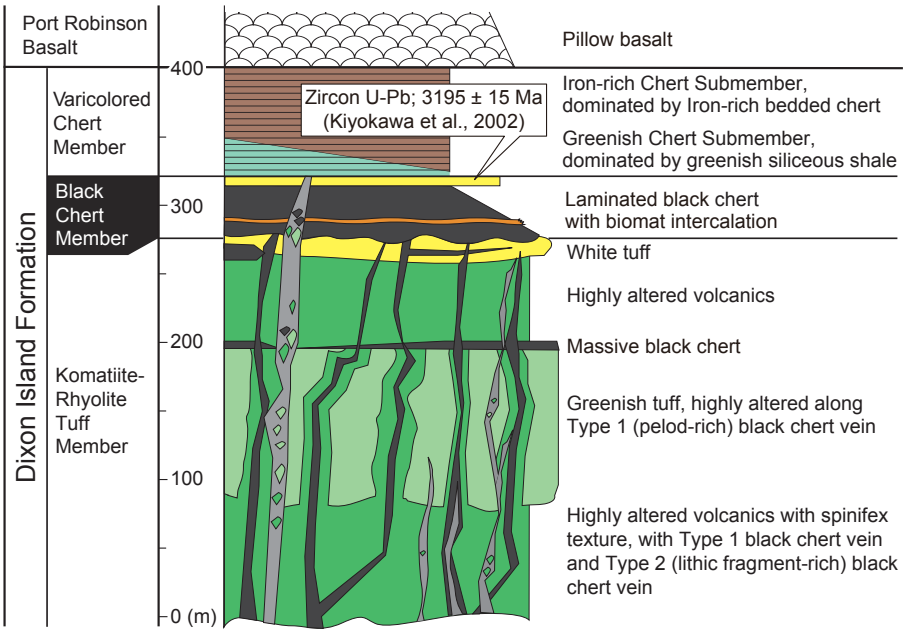

Figure 2: A stratigraphic column of the Dixon Island Formation, simplified after Kiyokawa et al. (2012, 2014).

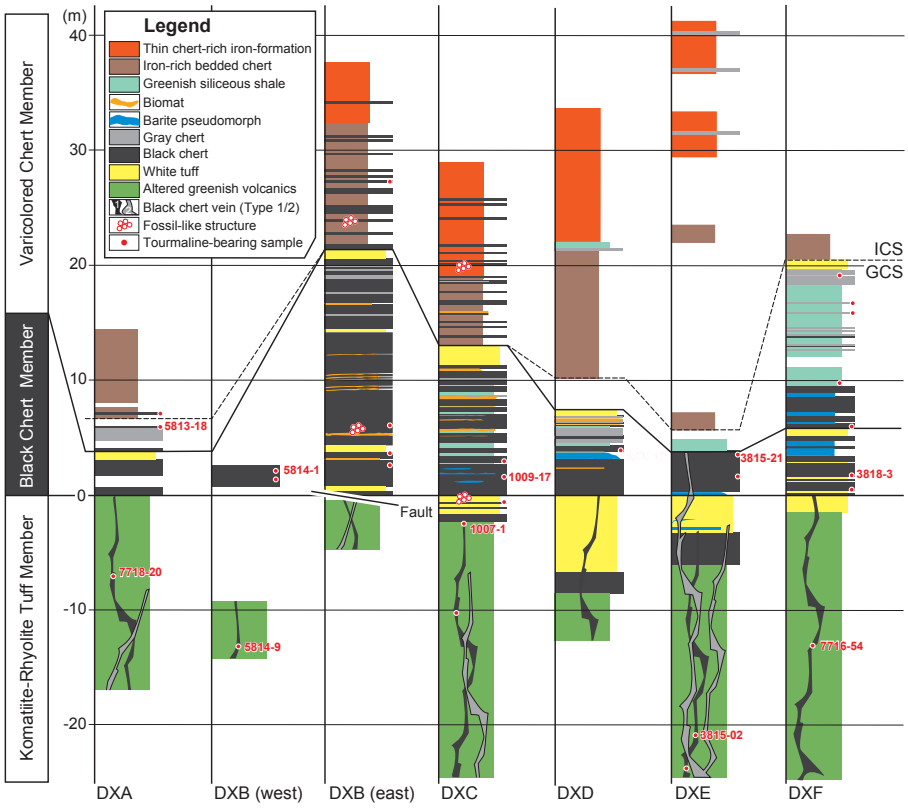

Figure 3: Stratigraphic columns of the geological blocks of DXA, DXB, DXC, DXD, DXE, and DXF in the Dixon Island Formation, modified after Kiyokawa et al. (2006, 2012). ICS and GCS mean Iron-rich Chert Submember and Greenish Chert Submember of the Varicolored Chert Member, respectively. Red dots mark horizons of tourmaline-bearing samples; as for samples examined for chemical compositions of tourmalines, their numbers are also attached.

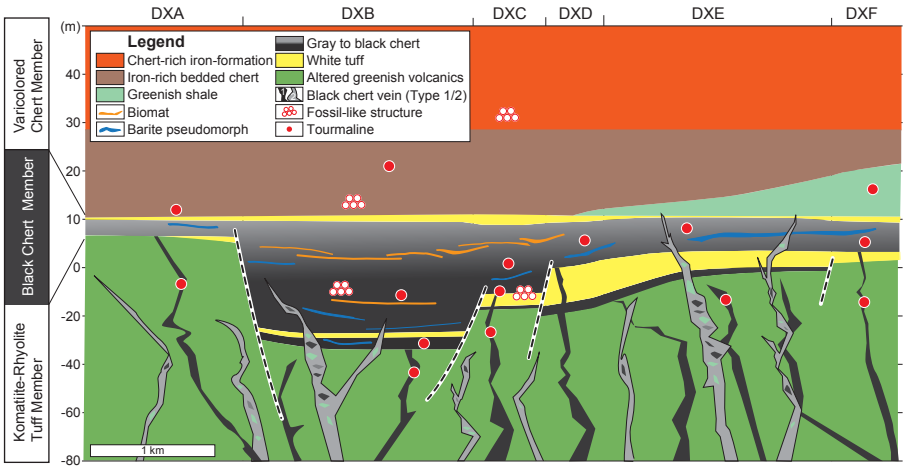

Figure 4: A model of the sedimentary environment of the Dixon Island Formation, modified after Kiyokawa et al. (2012). In the western blocks (DXB and DXC), the grabens developed are filled with massive black chert. In these deposits, tourmaline occurs not only as veins but also at the horizons below the intercalating biomats and fossil-like structures. The massive black chert is less dominant in the eastern blocks (DXE and DXF), where the Black Chert Member is penetrated by black chert veins, and covered with greenish siliceous shale of the Varicolored Chert Member.

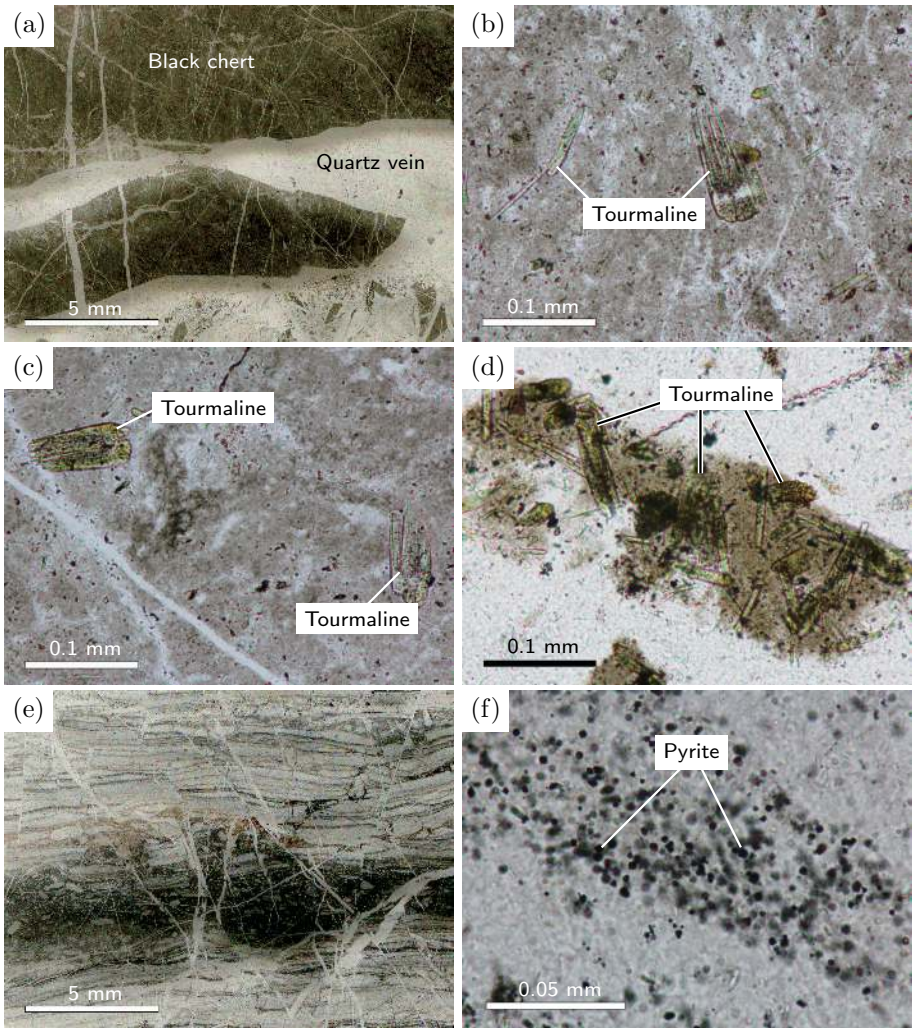

Figure 5: Optical images showing the textural characteristics of the black cherts. (a) Massive black chert, cut by quartz veins (DXA 5813-18). The quartz veins often contain fragments of massive black chert. (b) Acicular tourmaline in the carbonaceous matter-bearing matrix of the massive black chert (DXA 5813-18). (c) Acicular tourmaline in the carbonaceous matter-bearing black chert vein (DXB vein 5814-09). (d) A tourmaline-bearing fragment of the massive black chert, trapped in a quartz vein (DXF 7716-54). (e) The layered black chert, consisting of alternating white layers composed of microcrystalline quartz and black laminae dominated by pyrite (DXE 3815-21). The pyrite-dominant layers include rip-up crusts composed of microcrystalline quartz. (f) Pyrite granules in the black laminae (DXE 3815-21).

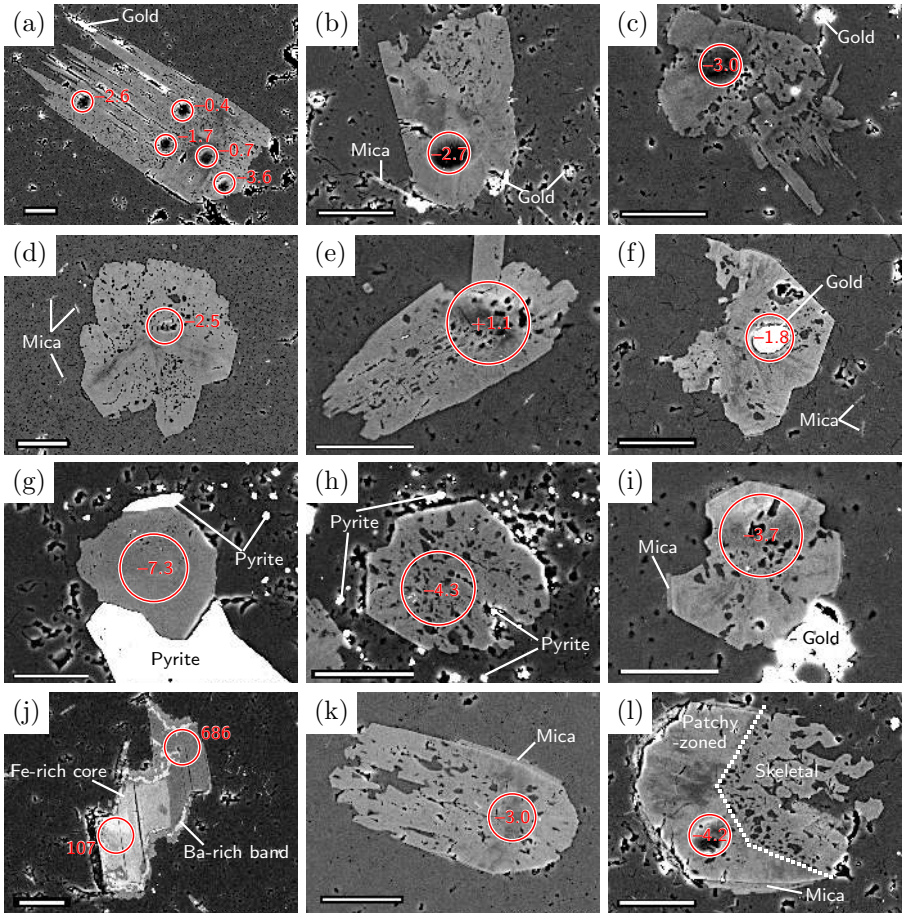

Figure 6: Back-scattered electron images showing the modes of occurrence of tourmaline and mica in the black cherts. Scale bars are 20 μm. The bright materials stuck in voids are the remains of the gold coat used for SIMS analysis. Red circles with numbers represent SIMS spots and δ^{11}B values obtained for tourmaline or $[B_2O_3]^{\mu g \cdot g^{-1}}$ for mica. See Tables 1 and 2 for chemical analyses on individual spots; (a) DXA 5813-18, spot T11-1∼T11-5, (b) DXA vein 7718-20, spot T13-1, (c) DXB 5814-01, spot T12-1, (d) DXB vein 5814-09, spot T02-1, (e) DXC 1009-17, spot T09-1, (f) DXC vein 1007-01, spot T02-1, (g) DXE 3815-21, spot T13-1, (h) DXE 3815-21, spot T16-1, (i) DXE vein 3815-02, spot T46-1, (j) DXE vein 3815-02, spot M35-1, M35-2, (k) DXF 3818-03, spot T08-1, and (l) DXF vein 7716-54, spot T05-1.

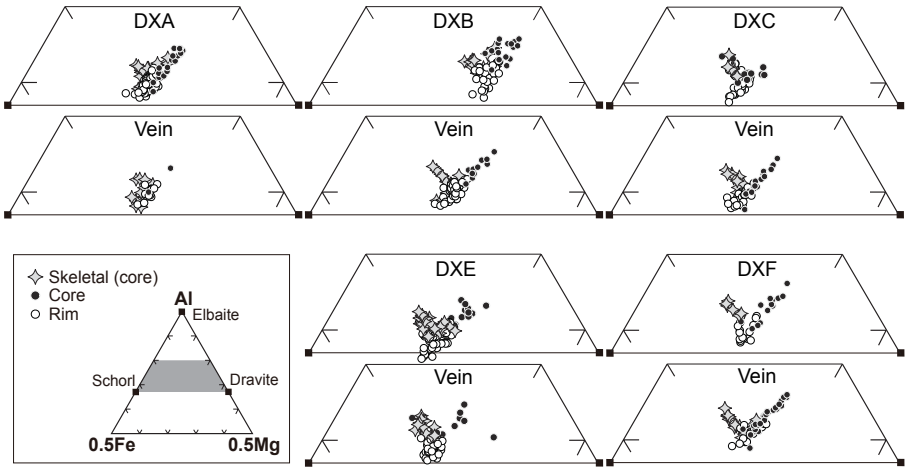

Figure 7: The major element compositions of tourmaline from black cherts, represented as a Al-Fe-Mg ternary system (Henry and Guidotti, 1985). In each diagram, a shaded domain of the ternary diagram (inset) is enlarged.

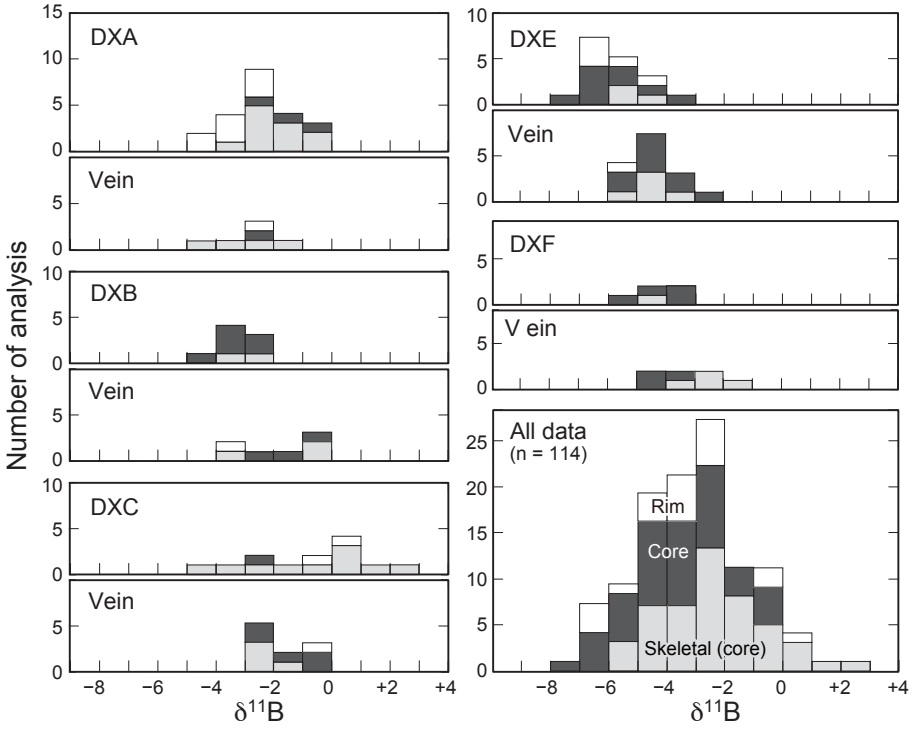

Figure 8: The boron-isotope compositions of tourmaline from the black cherts.

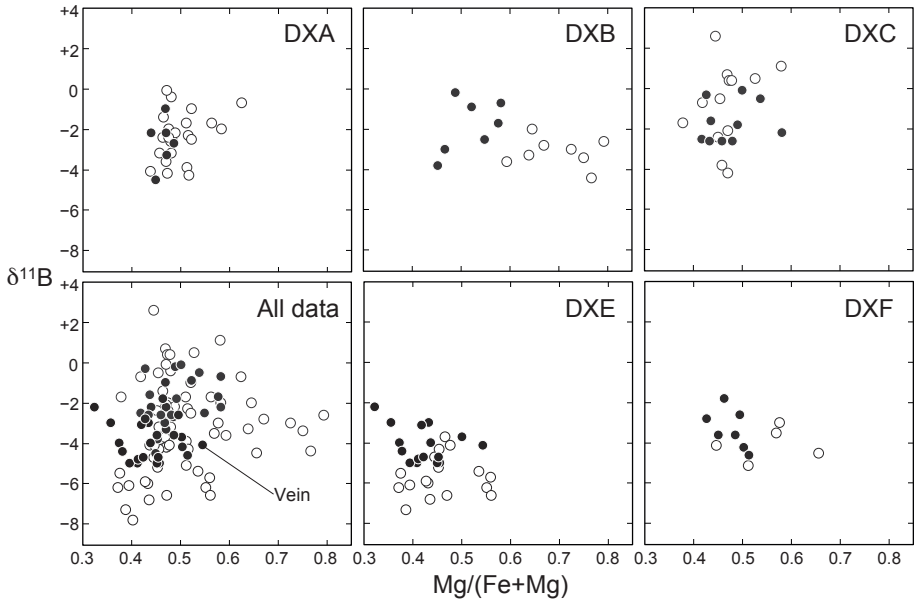

Figure 9: The major element and boron-isotope compositions of tourmaline from black cherts. Solid and open symbols show the compositions of tourmaline from black chert veins and the massive black chert, respectively.

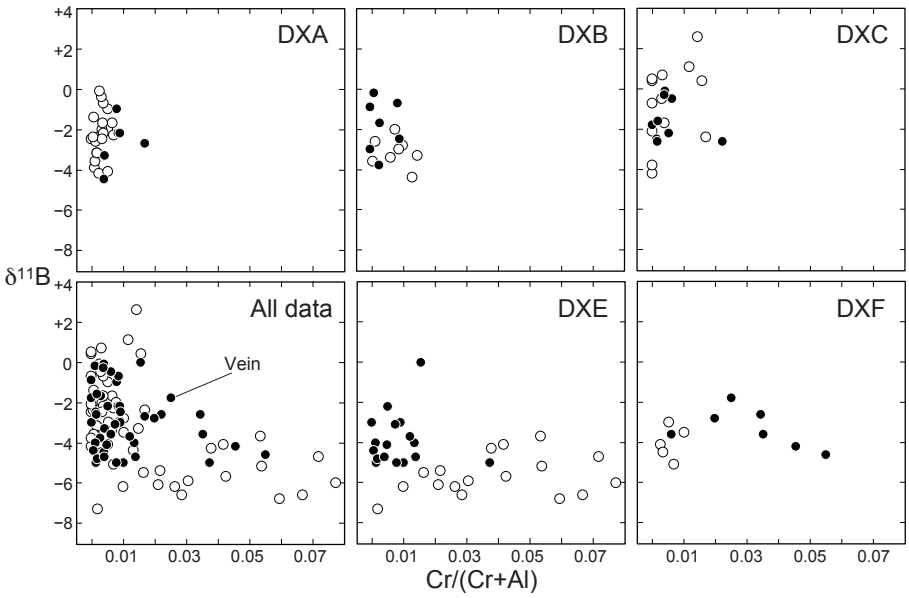

Figure 10: The minor element and boron-isotope compositions of tourmaline from black cherts. Solid and open symbols show the compositions of tourmaline from black chert veins and the massive black chert, respectively.

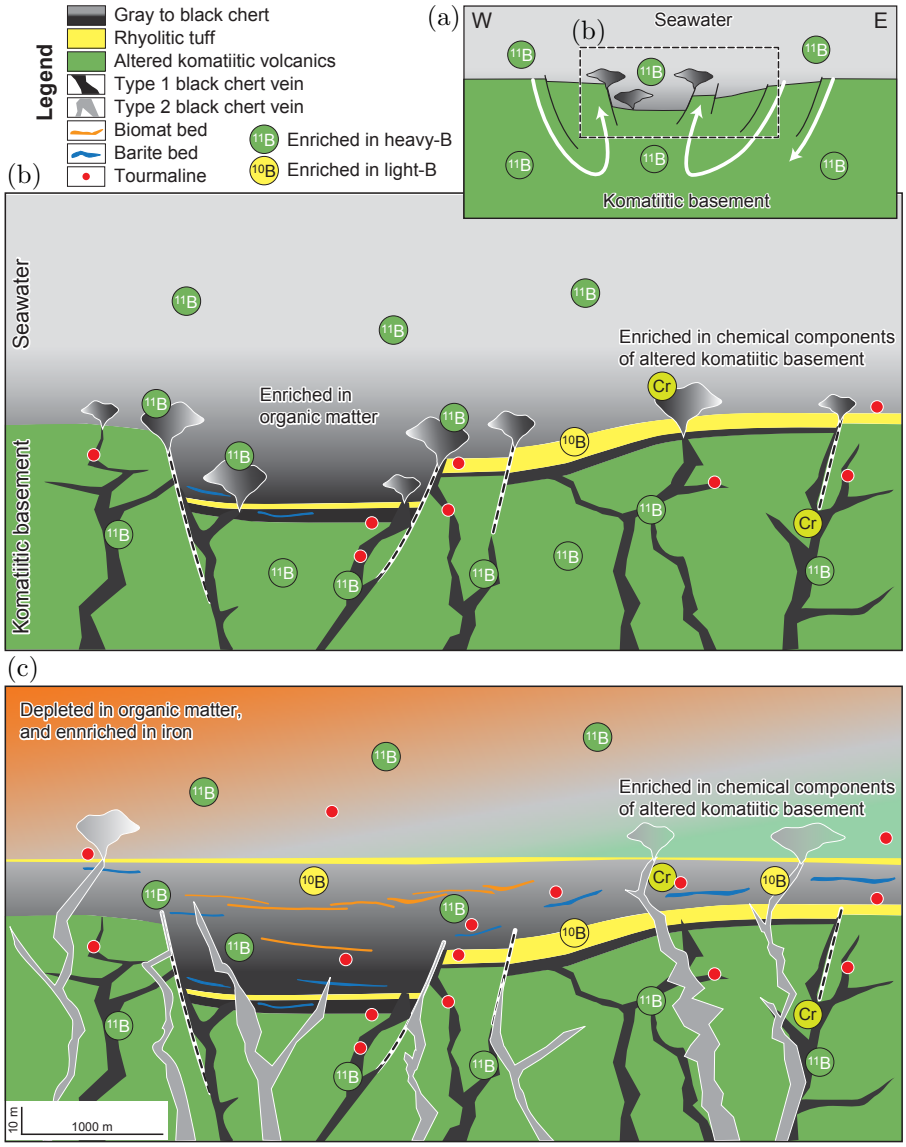

Figure 11: A model of the sedimentation history of the Black Chert Member and the Varicolored Chert Member from the Dixon Island Formation. (a) A panoramic view of the hydrothermal system. Seawater permeates into komatiitic basement along normal faults associated with grabens. The water interacts with wall-rocks, and rises back to the ocean floor as hydrothermal vent fluid. The site of (b) is indicated by a rectangle with dashed line. (b) Enlarged view of the hydrothermal system during the sedimentation of the Black Chert Member, with type 1 black chert vein activity. (c) Enlarged view of the hydrothermal system during the sedimentation of the Varicolored Chert Member, with type 2 black chert vein activity. In addition to organic matter, hydrothermal fluids are enriched in boron. In the Black Chert Member, tourmaline crystallized before biogenic mats developed. See text for details.